Quantum Fluids and Vortices

Carlo F. Barenghi
School of Mathematics and Statistics
Newcastle University

September 2009

Contents

Chapter 1

Motivation

1.1 Turbulence

These lectures are an introduction to world of quantum fluids and to phenomena which take place at very low temperatures near absolute zero: superfluidity, quantised vortices, Bose–Eintein condensation. The focus is on quantised vortices and quantum turbulence.

To motivate the study of quantum turbulence one has to appreciate the problem of turbulence in ordinary fluids first. Turbulence is not something which we experience only during bumpy flights. Turbulence is around us and inside us: the air in the room and the flow of blood in the aorta are turbulent. Turbulent flows range from tiny, gentle wakes created by a dragonfly (Fig. 1.1) to roaring pyroclastic flows caused by volcanic eruptions (Fig. 1.2).

Turbulence is perhaps the major unsolved problem of classical physics. Its difficulty arises from the nonlinearity of the governing Navier–Stokes equations. Another major difficulty is that turbulence involves a huge range of length scales.

Understanding turbulence is not only a challenge to our mathematical and physics understanding; it has also practical applications, ranging from engineering (flow around airfoils or inside jet engines) to atmospheric science (weather and climate models). The study of turbulence is therefore interdisciplinary, and involves mathematicians, physicists and engineers.

1.2 Vortices

The building block of turbulence are eddies (or swirls, or vortices). This fact was first recognized by Leonardo da Vinci, whose famous drawing of turbulent water consists of an ensemble of small swirls, see Fig. 1.3. By the way, vortices

have always fascinated artists. An example is the sea monster Charybdis, who lurked with another monster, Scylla, on either side of the Straits of Messina and threatened to swallop the ship of Ulysses in Homer's "Odyssey". Another example is the mytical Maelstrom, a swirl off the Lofoten Islands in Norway (Fig. 1.4), which was described by Edgar Allan Poe in the short story "A descent into the Maelstrom" and by Jules Verne in the novel "Twenty thosands leagues under the sea".

Vortices in ordinary fluids can be weak or strong, big or small. Examples are galaxies (Fig. 1.5), hurricanes (Fig. 1.6), tornadoes (Fig. 1.7) and wingtip vortices (Fig. 1.8).

Numerical simulations of classical turbulence show that a turbulent flow contains a great number of tubular regions where the vorticity $\boldsymbol{\omega} = \nabla \times \mathbf{v}$ is concentrated (Fig. 1.9).

The situation is simpler if we consider quantum fluids. These fluids are special fluids which exist only at very low temperature, near absolute zero, and which have undergone a phase transition called Bose–Einstein condensation. Although macroscopic, quantum fluids are governed by the laws of quantum mechanics rather than classical physics. Quantum mechanics introduces a strict constraint on the rotational motion, for which vorticity can only take the form of discrete, filamentary vortices, like mini-tornadoes, called vortex lines. Unlike classical vortices, the strength and the core structure of these quantum vortices is fixed, and the flow which spins about the axis is a superflow, thus it does not decay because there it does not suffer viscous forces like an ordinary fluids.

The turbulent state of such superfluid vortex lines is is therefore a tangle of filaments, as shown in Fig. 1.10. Despite being much simpler than ordinary turbulence, the vortex tangle shares some important properties with it. For example, recent studies suggest that in quantum turbulence the kinetic energy is distributed over the lengthscale according to the same celebrated Kolmogorov law of ordinary turbulence. The study of quantum turbulence is this not only exciting and interesting per se, but it may give us more insight into the difficult turbulence problem.

Figure 1.1: Turbulent flow created by a dragonfly (Adrian Thomas, Dept. Zoology, Oxford University)

.

Figure 1.2: Pyroclastic flow generated by the Mayon Volcano, Philippines, 1984.

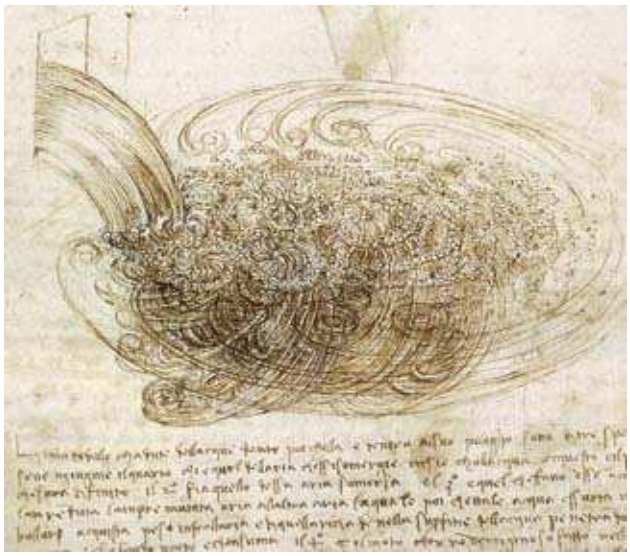

Figure 1.3: Leonardo da Vinci's drawing of turbulence generated by a small waterfall.

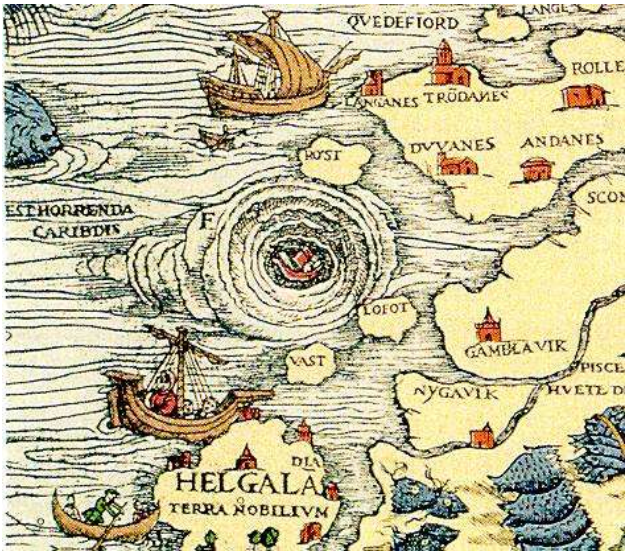

Figure 1.4: The Maelstrom in Olaus Magnus's Carta Marina (1539), University of Tromso, Norway.

Figure 1.5: The Whirpool galaxy.

Figure 1.6: A hurricane.

Figure 1.7: Tornado.

Figure 1.8: Trailing vortices created by wingtips.

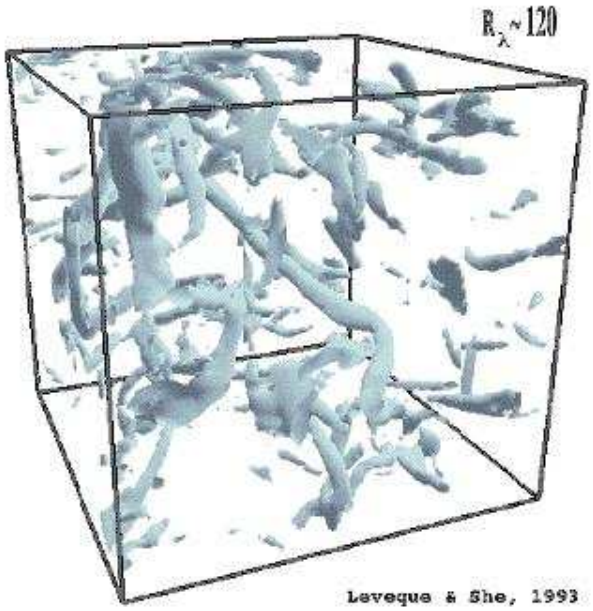

Figure 1.9: Regions of concentrated vorticity in numerical calculation of classical turbulence (E. Leveque)

.

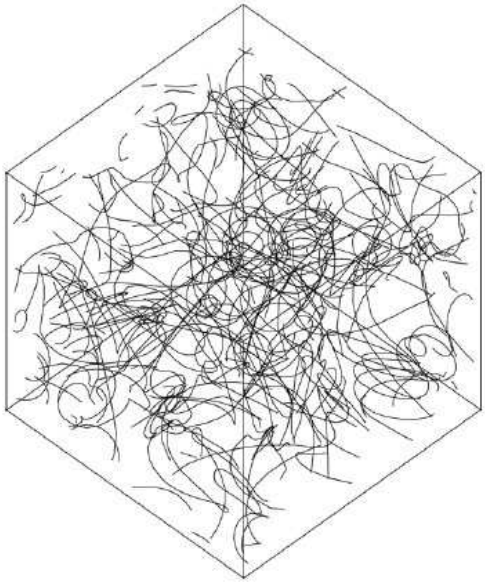

Figure 1.10: Tangle of quantum vortices in numerical calculation of quantum turbulence (CFB).

Chapter 2

Absolute Zero

2.1 The race to absolute zero

The first scientist who thought of an absolute zero of temperature was probably the French physicists and instrument maker **Guillaume Amontons** (1663-1705) (see Fig. 2.1). He measured the pressure of air at constant volume when the temperature was reduced (starting from the temperature of boiling water). He noticed that equal drops of temperature resulted in equal drops of pressure. Since, he argued, the pressure cannot become negative, further cooling would eventually bring the air to a state of zero pressure which would correspond to the lowest possible temperature. Amontons estimated that this temperature is -240 C. He thought that absolute zero should be a state of total rest, at which any motion has ceased.

This idea was further developed by the Swiss mathematician **Daniel Bernouilli** (1700-1782) (see Fig. 2.2), who postulated that all fluids consists of particles in constant irregular motion, continually colliding with each other (see Fig. 2.3). Since the collisions are elastic, he argued, this motion never runs down. Amontons and Bernouilli had the first insight into what is called now the kinetic theory of gases. They correctly interpreted the temperature of a gas as the average kinetic theory of the molecules. Unfortunately, the caloric theory of gases soon became very popular. According to this theory, proposed by the French chemist **Antoine Lavoisier** (the discoverer of oxygen), heat is a substance, called caloric which flows from one body to another.

During the XIX century the caloric theory was put aside, the study of heat developed greatly and the science of thermodynamics was born. Scientists realised that indeed there must be a limit to the degree of cold which is possible. Matter consists of particles (molecules and atoms), and tem-

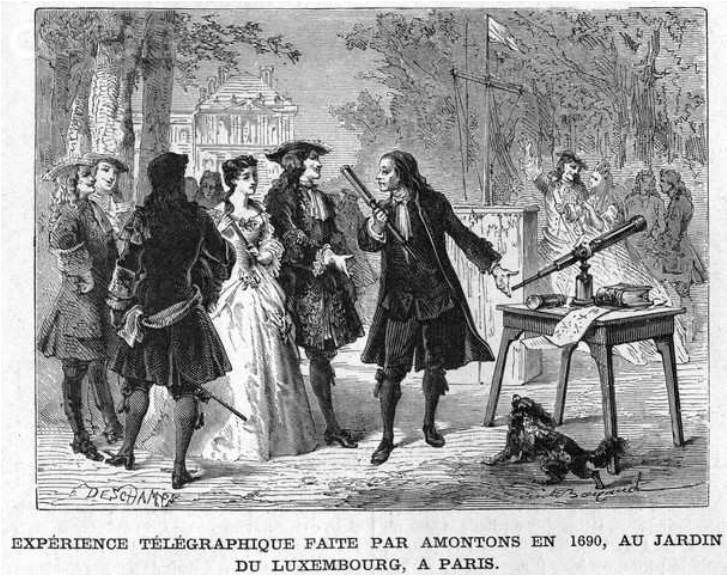

Figure 2.1: Guillaume Amontons.

perature measures their average velocity; therefore, if these particles can be brought to rest, temperature cannot be reduced any further, exactly as first envisaged by Amontons and Bernoulli. The interest in achieving lower and lower temperatures was also motivated by the fact that if the temperature is reduced there is less thermal disorder, hence the fundamental properties of matter become more apparent. The temperature scale which starts from the lowest possible temperature (absolute zero) is now called the Kelvin scale. One Kelvin degree is equal to one degree of the usual Centigrade scale, and absolute zero, $T = 0$ K, corresponds to $T = -273.15$ C.

Low temperature physics laboratories, competing against each other in the race toward absolute zero, developed techniques to liquefy all known gases, cooling matter to lower and lower temperatures. Oxygen was turned into a liquid at $T = 90$ K. Nitrogen required 77 K. In 1898 **James Dewar** (1842-1923) succeeded in liquefying hydrogen at $T = 20$ K (see Fig. 2.4). The only gas which resisted being liquefied was helium.

Although helium is the second most common element in the Universe, it was identified only in the late XIX century, first in the spectrum of solar radiation, and then, by **William Ramsay** (1852-1916), in rocks containing uranium. The competition between Dewar in London and his main rival, **Heike Kamerlingh Onnes** (1953-1926) in Leiden, was won by Onnes (Fig. 2.5), who succeeded in creating the first sample of liquid helium at $T = 4$ K in 1908. Three years later, in 1911, Onnes also discovered superconductivity,

Figure 2.2: Daniel Bernouilli.

which is the property of some metals (e.g. mercury, tin, lead) and alloys to sustain electrical currents without any electrical resistance. He was awarded the Nobel prize for this discovery.

2.2 Helium I and helium II

Onnes and his collaborator Dana found that liquid helium is transparent and that its density is $\rho = 0.145$ g/cm^3, approximately 1/6 of water's. They also noticed that liquid helium has unusual properties. Upon cooling the liquid helium by pumping on its vapour, the bubbling ceases when helium's temperature drops below a critical value (approximately 2 K); they found that the specific heat C_v has a sharp peak at the same temperature. They called the critical temperature T_λ, after the shape of the specific heat curve. The value of T_λ on the current Kelvin temperature scale is $T_\lambda = 2.1768$ K at saturated vapour pressure (SVP).

More experiments revealed that liquid helium below T_λ behaves very differently from liquid helium above it. The unusual low temperature liquid phase of helium was called helium II, to distinguish it from the high temperature liquid phase, called helium I. Helium II is a quantum fluid, whereas helium I is an ordinary fluid.

It is instructive to compare the phase diagram of an ordinary substance against that of liquid helium. In the case of an ordinary substance, see Figure 2.6, there is a point in the pressure vs temperature plane, called the triple point, which marks the equilibrium co-existence of gas, liquid and solid

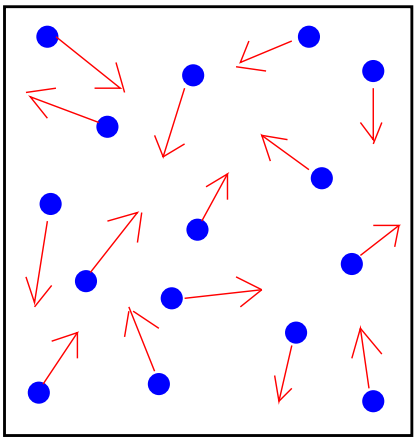

Figure 2.3: A gas consists of colliding molecules.

phases. In the case of liquid helium, see Figure 2.7, the triple point is missing, and the liquid phase extends down to absolute zero. To obtain solid helium, a large pressure (about 25 bars) must be applied. The boundary between helium I and helium II is called the lambda line; the intersection of the lambda line with the saturated pressure curve (along which most experiments are performed) is the lambda point.

The most striking property of helium II is superfluidity, which is the ability to flow without any viscous dissipation. Superfluidity was discovered independently by **Kapitza** and by Allen and Misener in 1938, for which (controversially) only Kapitza was awarded the Nobel prize. Superfluidity and superconducitvity are similar phenomena which could not be understood in the context of classical physics; both lacked a theoretical explanation for decades, although as early as 1938 **Fritz London** suggested a link between superfluidity and Bose–Einstein condensation, an effect speculated by Einstein and Bose in 1924.

2.3 Quantised vorticity

In the 1940's **Landau and Tisza** developed the two–fluid model, which accounts for the observed flow of helium II, at least at small velocities. Landau was awarded the Nobel prize for his work on superfluidity. The two–fluid model predicts an unusual mode of oscillation, called second sound to distinguish it from ordinary (first) sound; second sound was observed by Peshkov in 1941.

Experiments with rotating helium II revealed more surprises. The quanti-

Figure 2.4: James Dewar.

sation of the circulation, predicted by **Onsager** (1948) and **Feynman** (1955), both Nobel prize winners, explained these experiments. It became clear that quantum mechanics constrains the rotational motion of helium II to discrete mini–tornadoes (quantised vortex filaments). The quantum of circulation was actually observed by **Vinen** in 1961. Vinen also performed the first experimental investigations of quantum turbulence and developed the theory of mutual friction, which extends the two–fluid model to quantised vorticity. Quantum turbulence limits the otherwise ideal properties of helium II to transfer heat, so it is important in the engineering applications of liquid helium. Current research in helium II is concerned with the similarities and difference between classical turbulence and quantum turbulence.

2.4 ^{4}He and ^{3}He

The nucleus of ordinary helium (^{4}He) consists of two protons and two neutrons. Naturally occurring helium gas contains a small fraction (approximately 1 part in 10^7) of the rare isotope ^{3}He, whose nucleus contains only one neutron. In 1972 **Richardson, Lee and Osheroff** were awarded the Nobel prize for the discovery that pure liquid ^{3}He becomes superfluid too, but at much colder temperatures (of the order of few milliKelvins) than ^{4}He.

Figure 2.5: Self–portrait of Heike Kamerlingh Onnes.

2.5 Bose–Einstein condensation

The fundamental physical mechanism which is responsible for superfluidity is Bose–Einstein condensation (BEC). According to quantum mechanics, a particle has a characteristic wavelength, λ, associated with its momentum, p. In an ordinary gas, λ is much smaller than the average separation between the atoms of the gas, d. If the temperature of the gas is reduced, λ increases. At some critical temperature T_c, λ becomes of the order of d. In 1924 **Bose and Einstein** showed that a gas of non–interacting bosons (particles with integer spin) undergoes a phase transition at T_c. Phase transitions which we are more familiar with (e.g. the transition from water vapour to liquid water, or the transition from liquid water to ice) arise from the interaction between the molecules. The phase transition which Bose and Einstein identified is caused by the (quantum) statistics of the particles of the gas, not by their interaction, and takes place in momentum space rather than in physical space.

BEC in liquid helium is complicated by the fact that helium is a strongly interacting liquid, not the ideal gas of Bose and Einstein or a weakly interacting gas. Only in the 1990's, when techniques became available to trap and

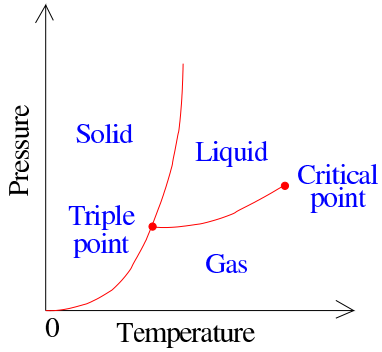

Figure 2.6: Phase diagram of an ordinary substance.

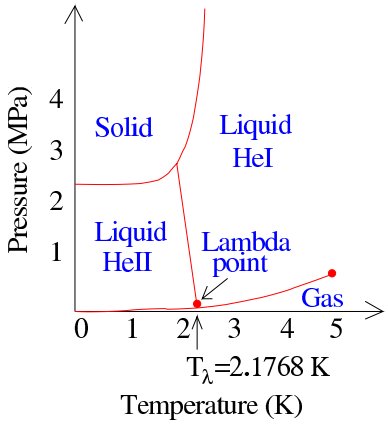

Figure 2.7: Phase diagram of liquid helium.

cool atomic gases using magnetic fields and lasers, Bose–Einstein condensation in its pure form was achieved experimentally by **Wiemann, Cornell and Ketterlee**, who were awarded the Nobel prize in 1995.

The following table gives an idea of the phenomena which take place at various order of magnitude for temperature.

K	item
10^{-10} K	Lowest temperature produced (in rhodium at Helsinki)
4.5×10^{-10} K	Sodium BEC (MIT)
2.5×10^{-3} K	Superfluid ^{3}He
1 K	Boomerang nebula
2.1768 K	Superfluid^{4}He
2.725 K	Cosmic microwave background radiation
4.1 K	Superconducting point of mercury
4.2 K	Boiling point of helium
7.2 K	Superconducting point of lead
14 K	Melting point of hydrogen
20 K	Boiling point of hydrogen
53 K	Mean temperature on Neptune
44 K	Mean temperature on Pluto
63 K	Melting point of nitrogen
68 K	Mean temperature on Uranus
77 K	Boiling point of nitrogen
90 K	Boiling point of oxygen
92 K	Superconducting point of Y-Ba-Cu-oxide (YBCO)
184 K	Coldest air recorded on Earth (−89 C)
195 K	Sublimation point of dry ice (carbon dioxide, −79 C)
210 K	Mean temperature on Mars (−63 C)
234 K	Melting point of mercury (−38 C)
273.15 K	Melting point of water (0 C)
278 K	Food refrigerators
287 K	Mean temperature on Earth (14 C)
293 K	Room temperature (20 C)
294 K	Lowest human body temperature survived
304 K	Melting point of butter (31 C)
310 K	Human body temperature (37 C)
315 K	Fatal human body temperature (42 C)
331 K	Hottest temperature recorded on Earth (58 C)
373.15 K	Boiling point of water (100 C)
1800 K	Melting point of iron
3680 K	Melting point of tungsten
3820 K	Melting point of diamond
5600 K	Earth's inner core boundary
5800 K	Surface of Sun
6000 K	Universe 300,000 years after Big Bang
13.6×10^6 K	Sun's core

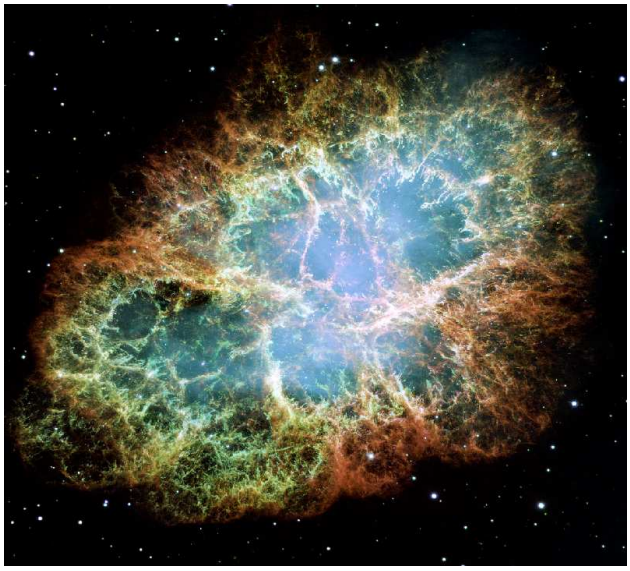

Figure 2.8: The Crab Nebula.

2.6 Neutron stars

Besides liquid ^{3}He, liquid ^{4}He and ultra–cold Bose–Einstein condensed atomic gases, there is a more exotic superfluid: neutron stars (also called pulsars). They are small (10 Km size) compact objects left over by supernova explosions Their interior consists of superfluid nuclear matter. The best–known pulsar is located at the centre of the Crab Nebula (Fig. 2.8). The Crab Pulsar is a source of gamma rays and radio waves. It is the remnant of the supernova explosion which was visible in daylight as recorded by Arab and Chinese astronomers in 1054.

2.7 Cryogenic engineering

The race toward absolute zero had a great impact on society. The techniques which were deeloped to produce low temperatures revolutionised the food industry (e.g. refrigerators).

Nowdays a common application of liquid helium is cooling superconducting magnets. The coils of these magnets are made of alloys which become superconducting if the temperature is less than a critical value. Superconducting magnets are routinely used in hospitals to make scans. They are also used in high energy physics laboratories to accelerate beams of elementary particles. An example is CERN's Large Hadron Collider (see Fig. 2.9). Along

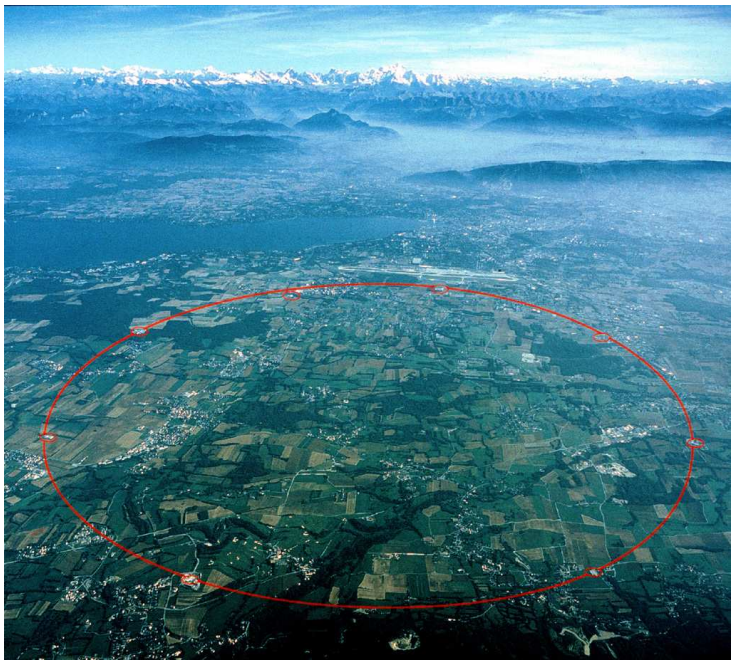

Figure 2.9: View of CERN, Lake Ginevra and the Alps. The circle denotes the location of the LHC.

the 27 km long ring of the LHC there are more than one thousand superconducting magnets; to provide a magnetic field strength of $80,000$ Gauss, each magnet is held at the operating temperature of $T = 1.8$ K. Liquid helium is also used by astrophysicists to cool infrared detectors; for example, the IRAS satellite (Fig. 2.10) carried 720 litres of liquid helium held at $T = 1.6$ K.

Figure 2.10: The IRAS satellite.

Chapter 3

Bose–Einstein Condensation

3.1 Waves

The wave character of matter has been at the heart of quantum mechanics since the early 1900's, when **Planck and Einstein** realised that light (more in general electromagnetic radiation) comes in discrete lumps, or packets, of energy

$$E = hf = \hbar\omega, \tag{3.1}$$

where f is the light's frequency, $\omega = 2\pi f$ the angular frequency, $h = 6.626 \times 10^{-27}\ erg\ s$ is Planck's constant, $\hbar = h/(2\pi)$ and $\tau = 1/f = 2\pi/\omega$ is the light's period. Following **de Broglie**, it became clear that a particle of momentum

$$p = mv, \tag{3.2}$$

where m is the mass and v the velocity, corresponds to a wave of wavelength

$$\lambda = \frac{h}{p}, \tag{3.3}$$

Another useful quantity is the wavenumber k, defined as $k = 2\pi/\lambda$. Thus $p = \hbar k$.

A 1–dimensional plane wave of amplitude A, wavenumber k and angular frequency ω has the form

$$\psi(x,t) = A\sin(kx - \omega t), \tag{3.4}$$

If we plot ψ as a function of t at fixed x, or ψ as a function of x at fixed t, we obtain a sinusoidal shape. If we "surf" with the wave we hold its phase

$\phi = kx - \omega t$ constant, hence $\Delta\phi = k\Delta x - \omega\Delta t = 0$, which means that we move with speed $v = \Delta x/\Delta t = \omega/k$. This quantity is called the phase speed of the wave.

3.2 Energy Levels

Let us consider for simplicity motion along the x direction only. According to quantum mechanics, a particle of mass m in the presence of a potential $V(x)$ obeys **Schroedinger's equation**

$$i\hbar\frac{\partial\Psi}{\partial t} = -\frac{\hbar^2}{2m}\frac{\partial^2\Psi}{\partial x^2} + V\Psi, \tag{3.5}$$

where the wavefunction $\Psi(x,t)$ (which is interpreted as a probability density) is normalised:

$$\int_{-\infty}^{\infty} |\Psi|^2 dx = 1. \tag{3.6}$$

Looking for solutions of the form $\Psi(x,t) = f(t)\psi(x)$, we separate the variables and obtain two equations:

$$i\hbar\frac{df}{dt} = Ef, \tag{3.7}$$

and

$$-\frac{\hbar^2}{2m}\frac{\partial^2\psi}{\partial x^2} + V\psi = E\psi, \tag{3.8}$$

where E is a separation constant. The first equation implies that

$$f(t) = e^{-iEt/\hbar} \tag{3.9}$$

hence $\Psi(x,t) = \psi(x)e^{-iEt/\hbar}$ where $\psi(x)$ is a solution of the second equation, which is an eigenvalue equation for ψ.

Let us suppose that the particle is free to move inside a box $-a \le x \le a$ but cannot escape from it; then the potential is an infinitely deep well of the form $V(x) = 0$ for $|x| < a$ and $V(x) = \infty$ for $|x| > a$. Inside the well the particle is free ($V = 0$), and the eigenvalue equation reduces to simply

$$-\frac{\hbar^2}{2m}\frac{\partial^2\psi}{\partial x^2} = E\psi, \tag{3.10}$$

The general solution is

$$\psi(x) = A\sin kx + B\cos kx, \tag{3.11}$$

where A and B are constant. If we impose the boundary conditions $\psi(\pm a) = 0$ we find two families of solutions: $\psi = B\cos kx$, which is even in x, and $\psi = A\sin kx$, which is odd in x, corresponding respectively to $k_n = \pm(n-1/2)\pi/a$ and $k_n = \pm n\pi/a$ and $\pm(n-1/2)\pi/a$, with $n = 1, 2, ...$ We also find that

$$E = \frac{\hbar^2 k^2}{2m}, \tag{3.12}$$

This equation shows the main result that, because of the discrete nature of k, the energy is quantised.

The energy levels which correspond to the even solutions are

$$E_n = \frac{\hbar^2\pi^2}{2ma^2}(n - \frac{1}{2})^2, \tag{3.13}$$

and the levels corresponding to the odd solutions are

$$E_n = \frac{\hbar^2\pi^2}{2ma^2}n^2, \tag{3.14}$$

where $n = 1, 2, ...$ The lowest energy level, called the ground state energy, is

$$E_1 = \frac{\hbar\pi^2}{8ma^2}. \tag{3.15}$$

3.3 Quantum Statistics

In the 1920's it became apparent that elementary particles are, in principle, not distinguishable from each other (in the way we distinguish ordinary particles from each other), and that they belong to two categories: fermions and bosons. What characterizes fermions and bosons is a quantum mechanical property called the spin. Bosons have integral spin (0, 1, etc in units of $\hbar$); examples of bosons are photons and ^{4}He atoms. Fermions have half integral spin (1/2, 3/2 etc in units of $\hbar$); examples of fermions are electrons, protons, neutrons and ^{3}He atoms. Fermions's wavefunctions are antisymmetric if one exhanges the coordinates of two particles, whereas bosons' are symmetric.

The distribution of particles in the accessible energy states for a system in thermal equilibrium is very different in the two cases. No fermion is allowed to occupy the same quantum state of another fermion, so there can be only one fermion on each energy level (Pauli's exclusion principle). This is the origin of the rules of chemistry and the periodic table of the elements. On the contrary, there is no constraint on the number of bosons which we can put in the same energy state.

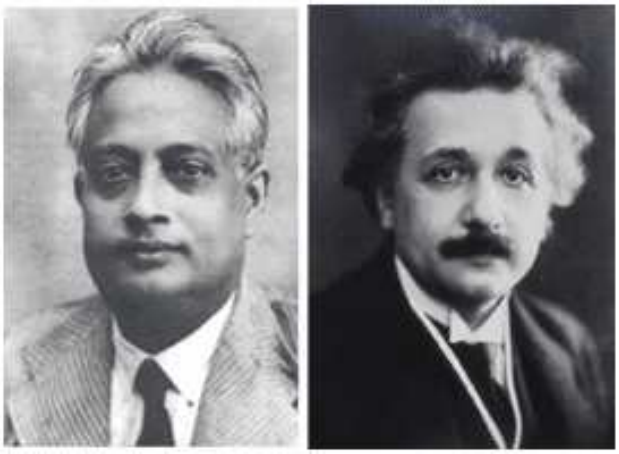

Figure 3.1: Satyendra Nath Bose (left) and Albert Einstein (right).

In 1924 a young Indian physicist from Decca called Bose wrote to Einstein, (who was already very famous) about his ideas on bosons. Einstein became interested, helped Bose in publishing his results, and worked on the problem. Bose and Einstein realised that if the temperature is sufficiently low, a gas of bosons behaves strangely: they discovered the phenomenon called Bose–Einstein condensation (BEC).

Suppose that we have a gas of only two particles, A and B, and that each particle can be in only three possible quantum states, $s = 1, 2, 3$. We distinguish between the classical Maxwell–Boltzmann statistics, which is responsible for ordinary thermodynamics, and two quantum statistics, called the Bose–Einstein and the Fermi–Dirac statistics:

- **Maxwell-Boltzmann.** In the case of an ordinary gas at room temperature we think that we can distinguish (label) each particle, at least in principle; particles are distinguishable, and can go into any quantum state. Fig. 3.2 (top) shows that there are 9 possible states for the whole gas.

- **Bose–Einstein.** If the particles are indistinguishable and any number of particles can be in any state, then we are in the situation described by Fig. 3.2 (middle): there are only 6 possible states for the whole gas.

- **Fermi–Dirac.** If the particles are indistinguishable and no more than one particle can be in any one state, then we have the situation of Fig. 3.2 (bottom): there are only 3 possible states for the whole gas.

Let P be the probability that two particles are found in the same state divided by the probability that two particles are found in different states.

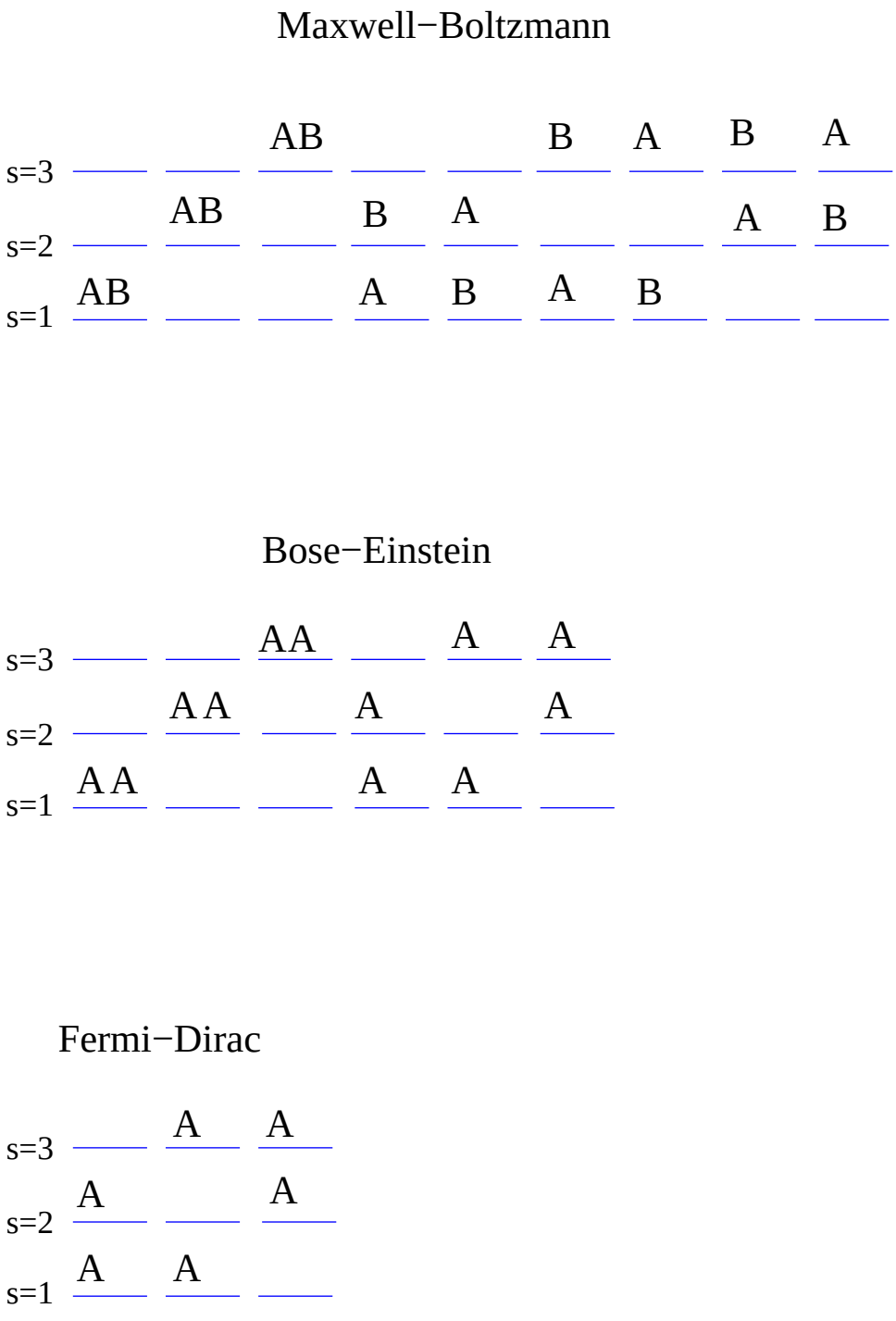

Figure 3.2: Maxwell–Boltzmann (top), Bose–Einstein (middle) and Fermi–Dirac (bottom) statistics of 2 particles, A and B, and 3 possible quantum states

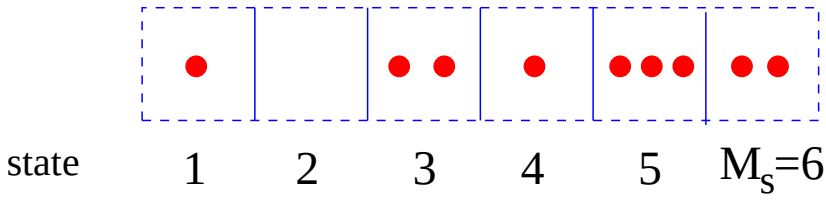

Figure 3.3: $N_s = 9$ particles and $M_s = 6$ levels

We have

$$P_{MB} = \frac{3/9}{6/9} = \frac{1}{2}, \tag{3.16}$$

$$P_{BE} = \frac{3/6}{3/6} = 1, \tag{3.17}$$

$$P_{FD} = \frac{0/3}{3/3} = 0. \tag{3.18}$$

We conclude that in the BE case there is a greater relative tendency for particles to "bunch up together" than in a classical system. Fermi–Dirac particles are the most "antisocial" of all, and avoid each other !

3.4 The Ideal Bose Gas

Suppose that we have N_s non–interacting particles which obey BE statistics and M_s available quantum states. We represent each state by a box rather than a level, and each individual particle by a dot, as in Fig. 3.3.

We want to count the number of possible available states for the whole gas. Note that we have N_s dots and $M_s - 1$ walls between the boxes which we can arrange along a line in any order. In each box we can put as many dots as we want. Essentially we have $N_s + M_s - 1$ objects (dots and walls) of which N_s are dots and $M_s - 1$ are walls.

If we had $N_s + M_s - 1$ distinguishable objects we could arrange them in $(N_s + M_s - 1)!$ ways. But we cannot distinguish a wall from a wall and a dot from a dot, so we must reduce the above number by $N_s!(M_s - 1)!$

We conclude that if we have N_s bosons and M_s quantum states the number of configurations in which we can arrange them is

$$W_s = \frac{(N_s + M_s - 1)!}{N_s!(M_s - 1)!}, \tag{3.19}$$

Consider a gas of N non–interacting bosons in the volume $V = L_x L_y L_z$. Each boson is in a plane–wave quantum state

$$\Psi(\mathbf{r}) = \frac{1}{V^{1/2}} e^{i\mathbf{k}\cdot\mathbf{r}}, \tag{3.20}$$

where $\mathbf{r} = (x, y, z)$, $\mathbf{k} = (k_x, k_y, k_z)$, and

$$\int_V |\Psi|^2 dV = 1, \tag{3.21}$$

Consider the x direction. To fit the boundary condition, the wavelength along x, λ_x, must be such that $n_x \lambda_x = L_x$; since $\lambda_x = 2\pi/k_x$, we have $k_x = 2\pi n_x / L_x$. Proceeding in the same way along y and z we conclude that the wavevector is

$$\mathbf{k} = (\frac{2\pi n_x}{L_x}, \frac{2\pi n_y}{L_y}, \frac{2\pi n_z}{L_z}), \tag{3.22}$$

Since $k_x = 2\pi n_x / L_x$, there are $\Delta n_x = (L_x/2\pi)\Delta k_x$ waves such that the wavenumber is in the range Δk_x. Thus the number of quantum states in the infinitesimal volume $d^3k = dk_x dk_y dk_z$ of k–space is

$$dn_x dn_y dn_z = \frac{L_x L_y L_z}{(2\pi)^3} dk_x dk_y dk_z = \frac{V}{(2\pi)^3} d^3k \tag{3.23}$$

Each of these single particles quantum states has energy

$$\epsilon_s = \frac{\hbar^2 k_s^2}{2m}. \tag{3.24}$$

Now consider the 3–dimensional k-space (see Fig. 3.4) and divide up the available single-particle states into a number of thin shells of thickness δk_s. The number of single-particle quantum states contained in a shell of radius k_s and thickness δk_s is

$$M_s = \frac{V}{(2\pi)^3} d^3k_s = \frac{V}{(2\pi)^3} 4\pi k_s^2 \delta k_s, \tag{3.25}$$

Using Eq. 3.24, we can express δk_s and k_s in terms of ϵ_s, and find that the number of available states between energy ϵ_s and $\epsilon_s + \delta\epsilon_s$ is

$$M_s = V D(\epsilon_s) \delta\epsilon_s, \tag{3.26}$$

where the function

$$D(\epsilon) = \frac{m^{3/2} \epsilon^{1/2}}{\sqrt{2}\pi^2 \hbar^3}, \tag{3.27}$$

is the density of states per unit volume.

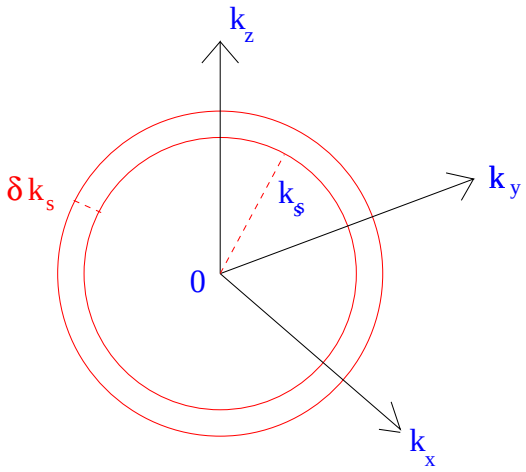

Figure 3.4: k–space

According to statistical physics, the entropy S of gas of N particles is

$$S = k_B \ln W, \tag{3.28}$$

where $k_B = 1.381 \times 10^{-16}\ erg/K$ is Boltzmann's constant and W is the number of available states of total energy E. To determine W we must find how the N atoms are distributed among the k–space shells of different energies.

Suppose that there are N_s bosons in the shell s. This shell contains M_s quantum states. From Eq. 3.19 we know that the number of available states for the whole shell is

$$W_s = \frac{(N_s + M_s - 1)!}{N_s!(M_s - 1)!}. \tag{3.29}$$

The total number of available states for the whole gas is simply the product of the number of available states in each shell:

$$W = \prod_s W_s = \prod_s \frac{(N_s + M_s - 1)!}{N_s!(M_s - 1)!}. \tag{3.30}$$

Substituting Eq. 3.30 into Eq. 5.3 we get

$$S = k_B \ln W = k_B \sum_s \ln \left(\frac{(N_s + M_s - 1)!}{N_s!(M_s - 1)!} \right), \tag{3.31}$$

To evaluate this expression we use the fact that $N_s >> 1$, $M_s >> 1$, then apply Stirling's formula $\ln x! \approx x \ln x - x$ for $x >> 1$. We obtain

$$S = k_B \sum_s \left((N_s + M_s) \ln (N_s + M_s) - N_s \ln N_s - M_s \ln M_s \right). \tag{3.32}$$

In thermal equilibrium the particles will distribute themselves so that the number N_s of particles in each energy shell will maximize the entropy S. The maximization of S must take place under the constraint that the total number of particles, N, and the total energy of the gas, E, are constant. We find

$$N_s = \frac{M_s}{e^{\beta(\epsilon_s - \mu)} - 1}. \tag{3.33}$$

The average number of particles occupying the state s is N_s/M_s:

$$n_s = \frac{N_s}{M_s} = \frac{1}{e^{\beta(\epsilon_s - \mu)} - 1}. \tag{3.34}$$

We conclude that in general the average number of particles in a state of energy ϵ is

$$n(\epsilon) = \frac{1}{e^{\beta(\epsilon - \mu)} - 1}, \tag{3.35}$$

The quantity $n(\epsilon)$ is called the occupation number. It can be shown that

$$\beta = \frac{1}{k_B T}, \tag{3.36}$$

and that μ is the chemical potential. The chemical potential appears in the first law of thermodynamics $dU = TdS - pdV + \mu dN$, where where p is the pressure.

It is useful to introduce the fugacity

$$z = e^{\beta\mu}, \tag{3.37}$$

and rewrite Eq. 3.35 as

$$n(\epsilon) = \frac{1}{z^{-1}\ e^{\beta\epsilon} - 1} \tag{3.38}$$

The lowest energy state, the ground state, has wavector $\mathbf{k} = 0$ and energy $\epsilon = 0$, hence its occupation number is

$$n(0) = \frac{1}{z^{-1} - 1} = \frac{z}{1 - z}, \tag{3.39}$$

Since $n(0)$ cannot be negative, we conclude that $z \leq 1$ and that the chemical potential is negative.

3.5 Condensation in Momentum Space

Using the Bose–Einstein distribution, Eq. 3.35, the total number of particles of the gas is

$$N = \sum_{\mathbf{k}} n(\epsilon_{\mathbf{k}}) = \sum_{\mathbf{k}} \frac{1}{e^{\beta(\epsilon_{\mathbf{k}}-\mu)} - 1}, \tag{3.40}$$

In the thermodynamic limit ($V \to \infty$) in which the density $n = N/V$ is held constant we replace the sum with an integral:

$$\sum_{\mathbf{k}} \to \int \frac{V}{(2\pi)^3} d^3k = \frac{V}{(2\pi)^3} \int_0^\infty 4\pi k^2 dk, \tag{3.41}$$

The particle density is thus

$$n = \frac{N}{V} = \frac{1}{(2\pi)^3} \int_0^\infty \frac{4\pi k^2 dk}{e^{\beta(\epsilon-\mu)} - 1} = \int_0^\infty \frac{1}{e^{\beta(\epsilon-\mu)} - 1} D(\epsilon) d\epsilon, \tag{3.42}$$

After some algebra we obtain

$$n = \left(\frac{m k_B T}{2\pi\hbar^2} \right)^{3/2} g_{3/2}(z), \tag{3.43}$$

which can be written

$$n = \frac{g_{3/2}(z)}{\lambda^3}, \tag{3.44}$$

where

$$\lambda = \left(\frac{h^2}{2\pi m k_B T} \right)^{1/2}, \tag{3.45}$$

is the thermal de Broglie wavelength. The function $g_{3/2}(z)$, shown in Fig. 3.5, is defined as

$$g_{3/2}(z) = \sum_{p=1}^{\infty} \frac{z^p}{p^{3/2}}, \tag{3.46}$$

The function $g_{3/2}$ has the following properties:

$$g_{3/2}(0) = 0, \qquad g_{3/2} \approx z \text{ for } z << 1, \tag{3.47}$$

$$g_{3/2}(1) = 2.612, \qquad \frac{dg_{3/2}}{dz}(1) = \infty. \tag{3.48}$$

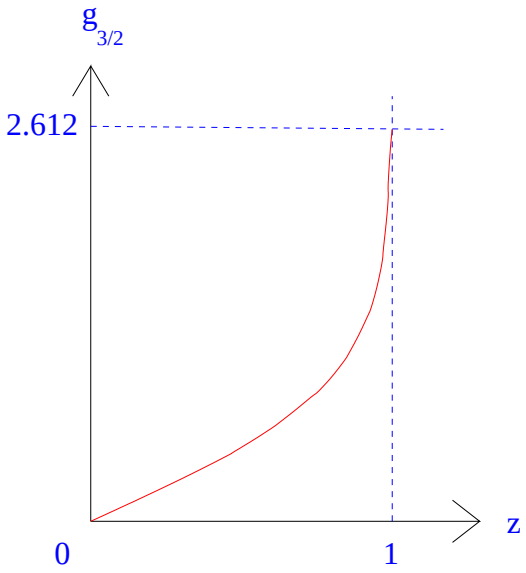

Figure 3.5: The function $g_{3/2}(z)$ vs z

Now we go to the heart of the matter. Consider the following inequality:

$$n = \frac{g_{3/2}(z)}{\lambda^3} \leq \frac{g_{3/2}(1)}{\lambda^3} = 2.612 \left(\frac{2\pi m k_B T}{h^3}\right)^{3/2}, \tag{3.49}$$

Eq. 3.49 shows that there is a problem in what we have done until now. Consider a gas of bosons of fixed density n. If we decrease T, eventually we reach a temperature T_c below which the inequality cannot be satisfied because the left hand side of Eq. 3.49 is fixed and the right hand side becomes too small. This critical temperature T_c, which corresponds to $z = 1$ and $\mu = 0$, is

$$T_c = \left(\frac{n}{2.612}\right)^{2/3} \frac{2\pi h^2}{m k_B}, \tag{3.50}$$

How to solve the problem ? Bose and Einstein noticed that in writing Eq. 3.41 we gave weight $4\pi k^2/(2\pi)^3$ to states with nonzero wavevector $\mathbf{k}$, and gave zero weight to the state with wavevector $\mathbf{k} = 0$, the ground state. But as T decreases, more and more bosons occupy the ground state because it has the lowest energy. The solution of the problem is that, in approximating the sum with an integral, the ground state must be treated separately. Thus Eq. 3.42 must be replaced by

$$n = \frac{n(0)}{V} + \frac{1}{(2\pi)^3} \int_0^\infty dk 4\pi k^2 n(\epsilon_{\mathbf{k}}) \tag{3.51}$$

where $n(0)$ is the occupation number of the ground state. The first term at the right hand side becomes important when $V \to \infty$ but $n(0)/V$ remains finite, that is, when a macroscopic fraction of bosons occupy the ground state. We have

$$n = \frac{n(0)}{V} + \frac{g_{3/2}(z)}{\lambda^3} = n_0 + \frac{g_{3/2}(z)}{\lambda^3}, \tag{3.52}$$

where

$$n_0 = \frac{n(0)}{V}. \tag{3.53}$$

is the density of bosons in the ground state.

Consider a gas with fixed n. At high T we can always choose z so that $n = g_{3/2}(z)/\lambda^3$ and $n_0 = 0$. But if we cool the gas, when $T < T_c$, it is necessary to have $n_0 > 0$. Since $n(0) = z/(1-z)$ we can write

$$n = \frac{z}{(1-z)}\frac{1}{V} + \frac{g_{3/2}(z)}{\lambda^3}, \tag{3.54}$$

If $T > T_c$ we can find a solution of this equation for $z < 1$; in the thermodynamic limit $V \to \infty$ the first term at the right hand side vanishes, so there are no bosons in the ground state.

As we cool the gas and let $T \to T_c$, we have $z \to 1$, and as $V \to \infty$, the first term at the right hand side of Eq. 3.54 remains finite to give the additional needed density n_0 at $T < T_c$, which is

$$\frac{z}{(1-z)}\frac{1}{V} = n_0 = n - \frac{g_{3/2}(1)}{\lambda^3}, \tag{3.55}$$

The temperature T_c is the critical temperature at which Bose–Einstein condensation takes place. Below T_c a gas has a finite density n_0 of particles in the ground state. The quantity n_0 is called the condensate's density, and the atoms in the ground state are called the condensate.

In summary, for $T \to T_c$ we have $z(T) \to 1$ and $\mu(T) \to 0$, whereas for $T \leq T_c$ we have $z(T) = 1$ and $\mu(T) = 0$.

Consider Eq. 3.55:

$$n_0 = n - \frac{g_{3/2}(1)}{\lambda^3} = n - 2.612 \left(\frac{2\pi m k_B T}{h^2}\right)^{3/2}, \tag{3.56}$$

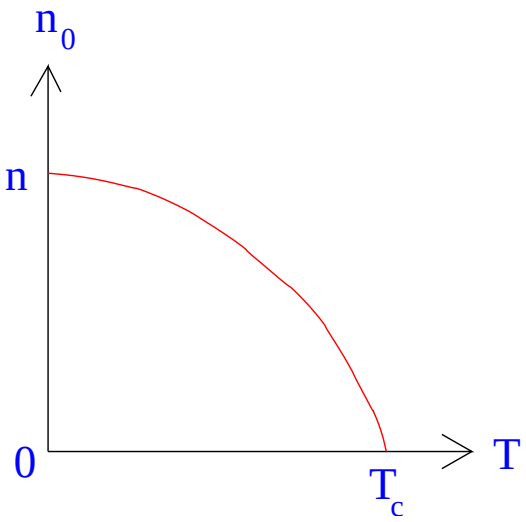

Figure 3.6: Density n_0 vs T

From Eq. 3.50 we have

$$n = 2.612 T_c^{3/2} \left(\frac{2\pi m k_B}{h^2} \right)^{3/2}, \tag{3.57}$$

hence

$$n_0 = n \left(1 - \left(\frac{T}{T_c} \right)^{3/2} \right). \tag{3.58}$$

This result is shown in Fig. 3.6. If $T = 0$ all the particles are in the ground state ($n = n_0$); increasing T put more and more particles in states of higher energy, until, at $T = T_c$, the condensate's density is zero: $n_0 = 0$.

Using these results one can compute the total internal energy of the gas, U, and the average energy per particle, $u = U/N$. Then we can compute the specific heat

$$C_v = \frac{\partial u}{\partial T}, \tag{3.59}$$

The result is shown in Fig. 3.7: note the cusp at $T = T_c$.

3.6 BEC in ultra–cold atomic gases

Experiments in the 1930's showed that liquid helium (^{4}He) becomes a superfluid if cooled below a critical temperature $T_c \approx 2.2$ K. The atom of ^{4}He

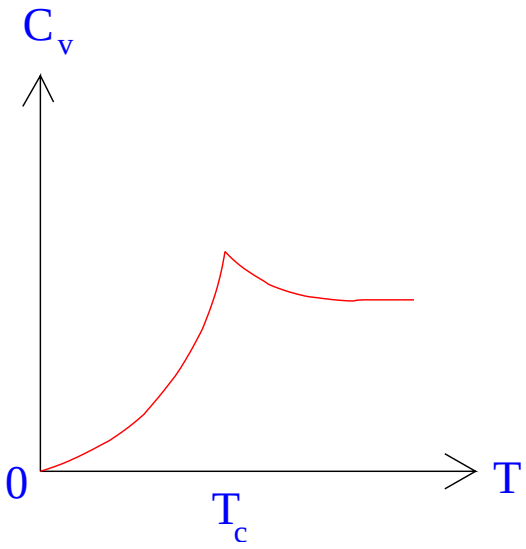

Figure 3.7: Specific heat C_v vs T

contains two protons and two neutrons in the nucleus surrounded by two electrons, so it is a boson with zero spin. Measurements of the specific heat C_v of liquid helium showed a spike at the critical temperature T_c, which is fairly close to the prediction of BEC in an ideal gas (using helium's parameters we would get $T_c = 3.1$ K). A relation between BEC and superfluidity was suggested by Fritz London. However, the fact that superfluid helium is a liquid with relatively high density means that that the interaction between the bosons cannot be neglected.

It was only in 1995 that BEC was realized in very dilute systems of atomic gases, in conditions similar to those envisaged by Bose and Einstein. This breakthrough was made possible by new techniques to trap and cool gases using lasers and magnetic fields. Fig. **??** shows velocity distributions of trapped ultra–cold atoms at temperature above the critical temperature T_c (left), just below T_c (middle) and well below T_c. The left figure shows the classical broad Maxwell–Boltzmann velocity distribution; the sharp peak which appears in the middle figure denotes that some atoms have zero velocity; the narrow peak in the right figure shows that almost all atoms have zero velocity. The figures are obtained by suddenly switching off the trap which confines the atoms. The distance the atoms move is measured by illuminating the atoms with a laser, hence their velocity can be inferred. The size of the Bose–Einstein condensates produced is small, of the order of 0.1 mm; the number od atoms in the condensate is typically 10^4 to 10^6, and the critical temperature T_c is of the order of 10^{-6} K.

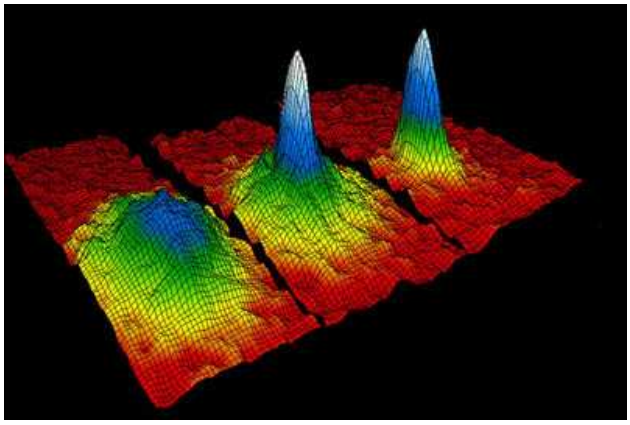

Figure 3.8: Velocity distributions of atoms for $T < T_c$ (left), just below T_c (middle) and well below T_c (right). The sharp peak at zero velocity marks the appearance of the condensate.

The gases which were found to undergo Bose–Einstein condensation consist of alakine atoms (lithium, sodium potassium, rubidium), in which there is a single electron in the outer energy orbital. Inner orbitals are full, with total orbital angular momentum and spin equal to zero. The only other contribution to the total spin of the atom is from the nucleus. If the sum of protons and neutrons is an odd number, the spin will be half–integer. In this case the sum of the nuclear spin and the spin of the valence electron will be an integer, so the atom will be a boson.

The gases in questions are different from the ideal gas of the theory of Bose and Einstein because they interact rather strongly, repelling each other almost as hard balls at short distances. Since these collision events are relatively rare, the atoms of the gases do not form clusters of atoms. Moreover, these interactions are events involving only two atoms, as three–body interactions are extremely rare. The two–body interaction of atoms can be described by the potential

$$V(\mathbf{r}_1 - \mathbf{r}_2) \approx g\delta(\mathbf{r}_1 - \mathbf{r}_2), \tag{3.60}$$

where δ is Dirac's delta function. Essentially the interaction is controlled by the parameter

$$g = \frac{4\pi a\hbar^2}{m}, \tag{3.61}$$

where a is called the s–wave scattering length. In most cases a and g are positive, which corresponds to repulsive interaction between the bosons.

In can be shown that the such relatively weakly interacting Bose gases undergo the same transition as an ideal gas of bosons. In the limit of zero temperature the gas is governed by the **Gross–Pitaevskii equation** (GP):

$$i\hbar\frac{\partial\Psi}{\partial t} = -\frac{\hbar^2}{2m}\nabla^2\Psi + g\Psi|\Psi|^2 + V_{trap}\Psi, \tag{3.62}$$

The equation contains the mean–field contribution to the interaction potential $V(\mathbf{r}) = gn(\mathbf{r}) = g|\Psi(\mathbf{r})|^2$, where $n(\mathbf{r})$ is the density

$$n(\mathbf{r}) = |\Psi(\mathbf{r})|^2, \tag{3.63}$$

and $V_{trap}(\mathbf{r})$ is the potential which confines the atoms. The GP equation is also called the Nonlinear Schroedinger Equation (NLSE) because it is a Schroedinger equation with cubic nonlinearityi; the potential depends on the particle density $n(\mathbf{r})$ which depends on the wave function $\Psi(\mathbf{r})$ itself.

The solution of the GP equation is normalised by the condition that the total number of atoms in the trap is N:

$$\int |\Psi(\mathbf{r})|^2 d^3\mathbf{r} = N. \tag{3.64}$$

Chapter 4

The GP Equation

4.1 Inhomogeneous condensate

We have seen that a trapped atomic BEC consiting of an ultra cold gas is described by the GP equation 3.62 for $\Psi(\mathbf{r}, t)$.

$$i\hbar\frac{\partial\Psi}{\partial t} = -\frac{\hbar^2}{2m}\nabla^2\Psi + g\Psi|\Psi|^2 + V_{trap}\Psi, \tag{4.1}$$

Assuming

$$\Psi(\mathbf{r}, t) = \psi(\mathbf{r}, t)e^{-i\mu t/\hbar}, \tag{4.2}$$

where μ is called the chemical potential, or energy per boson, the GP equation becomes

$$i\hbar\frac{\partial\psi}{\partial t} = -\frac{\hbar^2}{2m}\nabla^2\psi + g\psi|\psi|^2 + V_{trap}\psi - \mu\psi, \tag{4.3}$$

where ψ is normalised by the condition that the total number of atoms in the trap is N:

$$\int |\Psi(\mathbf{r})|^2 d^3r = N. \tag{4.4}$$

This is the case of the inhomogeneous condensate, because (as we shall see) the density of the condensate in the trap is not constant, and depends very much on the position.

4.1.1 Fermi–Thomas approximation to the ground state

Consider the harmonic, spherically symmetric potential

$$V_{trap} = \frac{m\omega_{trap}^2 r^2}{2}, \tag{4.5}$$

where $r^2 = x^2 + y^2 + z^2$ is the radius in spherical coordinates and ω_{trap} is the trap's frequency. For a sufficiently large cloud of atoms, an approximate solution ψ_{FT} for the ground state ψ_0 can be obtained by assuming $\partial/\partial t = 0$ and by neglecting the first term at the right hand side of Eq. 4.3; assuming that ψ is real, we find

$$g\psi^3 + V_{trap}\psi - \mu\psi = 0, \tag{4.6}$$

The solution is

$$\psi_{FT} = \begin{cases} \sqrt{(\mu - V_{trap})/g} = \sqrt{m\omega_{trap}^2(r_{FT}^2 - r^2)/(2g)} & r \le r_{FT} \\ 0 & r > r_{FT} \end{cases} \tag{4.7}$$

This approximation is called the Fermi-Thomas approximation. The Fermi–Thomas radius r_{FT} is given by the condition $\mu - V_{trap} = 0$, thus

$$\mu = \frac{m\omega_{trap}^2 r_{FT}^2}{2}. \tag{4.8}$$

To relate r_{FT} and to N we apply the normalization

$$\int d^3\mathbf{r}|\psi|^2 = N. \tag{4.9}$$

We find

$$4\pi \int_0^\infty dr\ r^2|\psi|^2 = 4\pi \int_0^{r_{FT}} dr\ r^2 \frac{m\omega_{trap}^2}{2g}(r_{FT}^2 - r^2) = N, \tag{4.10}$$

from which we get

$$r_{FT} = \left(\frac{15N\hbar^2 a}{m^2\omega_{trap}^2}\right)^{1/5}. \tag{4.11}$$

Finally we relate μ to N:

$$\mu = \frac{m\omega_{trap}^2}{2}\left(\frac{15N\hbar^2 a}{m^2\omega_{trap}^2}\right)^{1/5}. \tag{4.12}$$

The same analysis can be sone in the simpler case of the two–dimensional and the one–dimensional condensates, $\psi = \psi(x, y)$ and $\psi = \psi(x)$.

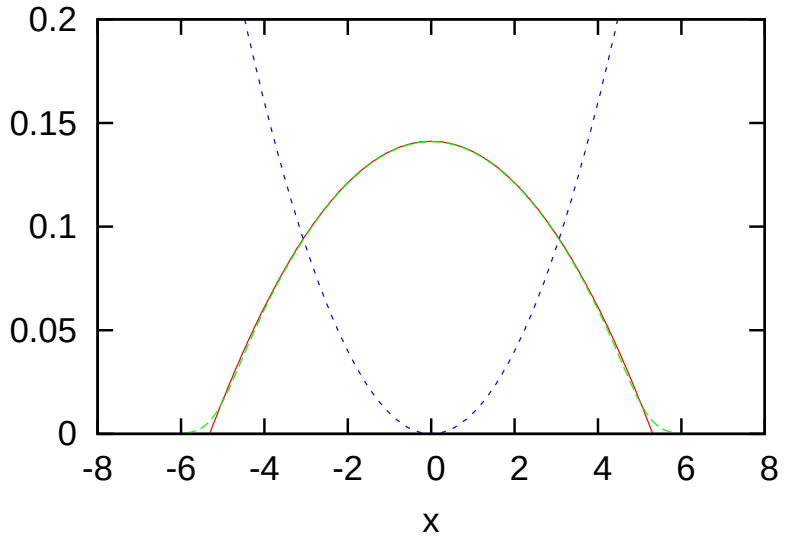

Figure 4.1: The Fermi–Thomas approximation $\psi_{FT}(x)$ (red curve), the exact ground state $\psi_0(x)$ (green curve), and the trapping potential $V_{trap}(x)$ (dashed blue line).

4.1.2 Ground state

The exact ground state solution $\psi_0(\mathbf{r})$ of Eq. 4.3 must be found numerically. It is not much different from the Fermi–Thomas approximation $\psi_{FT}(\mathbf{r})$: the main difference is that it decays slowly at the edge of the condensate, rather than suddenly becoming zero at the Fermi–Thomas radius.

Fig. 4.1 illustrates the difference between the Fermi-Thomas approximation and the exact ground state solution ψ_0 in a one–dimension condensate.

4.1.3 Quantisation of the circulation

We have seen that at sufficiently small temperatures the single particle wavefunction $\psi_0 = e^{-i\mathbf{k}\cdot\mathbf{r}}/\sqrt{V}$ with $\mathbf{k} = 0$ becomes occupied with a macroscopic number of particles. This wavefunction, $\psi_0 = 1/\sqrt{V}$, is constant. In quantum mechanics the wavefunction is defined up to an arbitray phase factor θ, so $\psi_0 = e^{i\theta}/\sqrt{V}$ is an equally valid solution. However, if $\theta = \theta(\mathbf{r})$, that is to say θ varies in space, the situation is different and we have a superflow.

Let us write $\psi_0(\mathbf{r})$ in terms of its amplitude, $\sqrt{n_0(\mathbf{r})}$, and its phase, $\theta(\mathbf{r})$:

$$\psi_0(\mathbf{r}) = \sqrt{n_0(\mathbf{r})}e^{i\theta(\mathbf{r})}. \tag{4.13}$$

According to quantum mechanics, the current density (the number of particles flowing per unit area per unit time) is

$$\mathbf{j}_0 = \frac{\hbar}{2im}(\psi_0 \nabla \psi_0^* - \psi_0^* \nabla \psi_0), \tag{4.14}$$

We obtain

$$\mathbf{j}_0 = \frac{\hbar}{m} n_0 \nabla \theta. \tag{4.15}$$

.

Since $\mathbf{j}$ has the dimensions of a density times a velocity, we define the superfluid velocity as

$$\mathbf{v}_s = \frac{\hbar}{m}\nabla\theta, \tag{4.16}$$

We shall see that this flow is a movement of particles without dissipation of energy, unlike what happens in an ordinary flow.

Note that, since the curl of a gradient is always zero, the superflow is irrotational:

$$\nabla \times \mathbf{v}_s = 0, \tag{4.17}$$

Now consider the circulation of $\mathbf{v}_s$ along a closed path C:

$$\Gamma = \oint_C \mathbf{v}_s \cdot \mathbf{dr}, \tag{4.18}$$

If C is a simply connected region, we apply Stokes's Theorem, use $\nabla \times \mathbf{v}_s = 0$, and conclude that

$$\Gamma = \oint_C \mathbf{v}_s \cdot \mathbf{dr} = \int_S \nabla \times \mathbf{v}_s \cdot \mathbf{dS} = 0. \tag{4.19}$$

where S is the surface enclosed by th path C. If C is is multiply connected region, Stokes's Theorem is invalid, and we have

$$\Gamma = \oint_C \mathbf{v}_s \cdot \mathbf{dr} = \frac{\hbar}{m} \oint_C \nabla\theta \cdot \mathbf{dr} = \frac{\hbar}{m}\Delta\theta, \tag{4.20}$$

where $\Delta\theta$ is the change of the phase θ as we go around the path C. But the wavefunction must be defined in a unique way, so

$$\psi_0(\mathbf{r}) = \psi_0(\mathbf{r})e^{i\Delta\theta}, \tag{4.21}$$

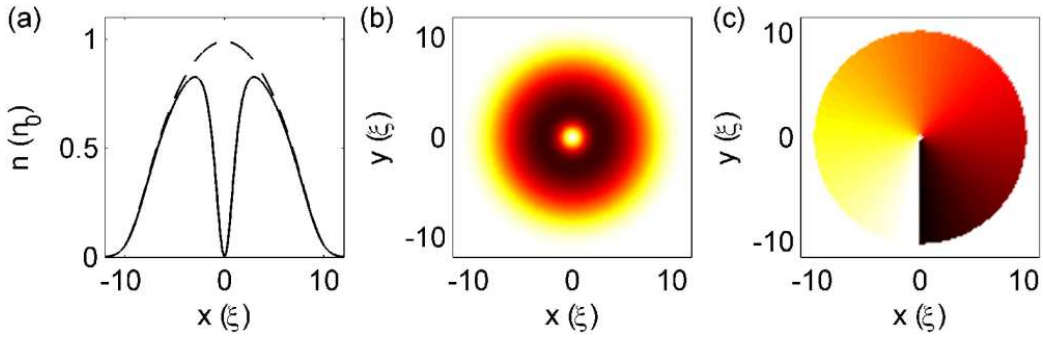

Figure 4.2: Left: profile of a 2–dimenensional trapped BEC with (solid) and without (dashed) a vortex. Middle: density $n(x, y)$ in the x, y plane. Right: phase $\theta(x, y)$ in the x, y plane.

thus $\Delta\theta = 2\pi n$ where n is an integer. We conclude that the circulation Γ is quantised in units of the quantum of circulation $\kappa = h/m$:

$$\Gamma = \frac{h}{m} n = n\kappa, \qquad (n = 1, 2, \cdots) \tag{4.22}$$

This important result makes the superflow very different from an ordinary flow, in which the circulation can take any arbitrary value.

Fig. 4.2 shows the profile of a trapped 2–dimensional condensate with and without a vortex in the middle (left), the density $n(x, y)$ (middle) and the phase (right) in the x, y plabe. Note that on the axis of the vortex the density is zero.

4.1.4 Dimensionless variables

It is convenient to write the GP equation in dimensionless for. In this way the number of independent parameters becomes apparent and the numerical solution can be computed avoiding numbers which are too big or too small.

The quantity

$$\delta = \left(\frac{\hbar}{m\omega_{trap}} \right)^{1/2}, \tag{4.23}$$

is called the harmonic oscillator's length. We use a prime to distinguish dimensionless variables (e.g. x' and t') from dimensional ones (e.g. x and t). We introduce

$$t = \frac{t'}{\omega_{trap}}, \qquad x = x'\ \delta, \qquad y = y'\ \delta, \qquad z = z'\ \delta, \tag{4.24}$$

Derivatives are computed using the chain rule, for example

$$\frac{d\psi}{dx} = \frac{d\psi}{dx'}\frac{dx'}{dx} = \frac{1}{\delta}\frac{d\psi}{dx'}. \tag{4.25}$$

$$\frac{d}{dt} = \omega_{trap}\frac{d}{dt'}, \qquad \nabla^2 = \frac{1}{\delta^2}\nabla'^2, \tag{4.26}$$

Note that ∇'^2 contains derivatives with respect to x', y', z', whereas ∇ contains derivatives with respect to x, y, z. The normalization condition Eq. 4.4 suggests the introduction of

$$\psi' = \psi\left(\frac{\delta^3}{N}\right)^{1/2}, \tag{4.27}$$

Eq. 4.4 becomes

$$\int dx'\ dy'\ dz'|\psi'|^2 = 1, \tag{4.28}$$

and the GP equation becomes

$$i\frac{\partial\psi'}{\partial t'} = \left(-\frac{1}{2}\nabla'^2 + C|\psi'|^2 + V'_{trap} - \mu'\right)\psi', \tag{4.29}$$

where

$$C = \frac{4\pi N a}{\delta}, \qquad \mu' = \frac{\mu}{\hbar\omega_{trap}}, \qquad V'_{trap} = \frac{r'^2}{2} \qquad r' = \frac{r}{\delta}. \tag{4.30}$$

4.2 Homogeneous condensate

The GP equation is also a convenient model of superfluid helium. Since helium experiments usually involve large numbers of atoms (many liters of liquid in some cases), it is useful to learn properties of the solutions of the GP equations which do not depend on a specific trapping potential V_{trap}, which we set equal to zero. This is the case of the homogeneous condensate: apart from small regions near the walls of the container, the condensate's density is constant. The governing GP equation is

$$i\hbar\frac{\partial\psi}{\partial t} = -\frac{\hbar^2}{2m}\nabla^2\psi + g\psi|\psi|^2 - \mu\psi, \tag{4.31}$$

4.2.1 Uniform solution

The simplest solution of the homogeneous GP equation is that of a uniform condensate, for which the solution ψ_∞ does not depend on t or $\mathbf{r}$. Assuming that ψ_∞ is real, Eq. 4.31 reduces to

$$g\psi_\infty^3 - \mu\psi_\infty = 0, \tag{4.32}$$

The solution is

$$\psi_\infty = \sqrt{\mu/g}, \tag{4.33}$$

hence the number density is $n_\infty = |\psi_\infty|^2 = \mu/g$.

4.2.2 Healing Length

The characteristic lenghscale ξ over which ψ changes in space is obtained by balancing the kinetic energy and the interaction terms in Eq. 4.31. Replacing $\partial^2\psi/\partial x^2$ with ψ/ξ^2 where ξ is the lenghscale, we estimate

$$\frac{\hbar^2}{2m}\frac{\partial^2\psi}{\partial x^2} \approx \frac{\hbar^2}{2m}\frac{\psi}{\xi^2} = g|\psi|^2\psi = gn\psi, \tag{4.34}$$

hence

$$\xi = \frac{\hbar}{\sqrt{2mgn}}. \tag{4.35}$$

In a uniform condensate $n = \mu/g$ hence

$$\xi = \frac{\hbar}{\sqrt{2m\mu}}. \tag{4.36}$$

The quantity ξ is called the healing length.

4.2.3 Wall solution

The second simplest solution of the homogeneous GP equation is that of a steady ($\partial/\partial t = 0$), one–dimensional condensate in the presence of a wall, which obeys

$$-\frac{\hbar^2}{2m}\frac{\partial^2\psi}{\partial x^2} + g\psi|\psi|^2 - \mu\psi = 0, \tag{4.37}$$

in the range $0 \leq x < \infty$. The boundary condition $\psi(0) = 0$ represents an infinite potential barrier at $x = 0$; the second boundary condition is $\psi = \psi_\infty = \sqrt{\mu/g}$ at $x \to \infty$. The solution is

$$\psi(x) = \sqrt{\mu/g}\,\tanh(\frac{x}{2\xi}). \tag{4.38}$$

4.2.4 Waves

The GP equation sustain wave solutions. If the uniform condensate $\psi_\infty = \sqrt{\mu/g}$ is slightly disturbed, the dispersiona relation of perturbations of the form $e^{ikx-i\omega t}$, where k is the wavenumber and ω the angular frequency, is

$$\omega = \sqrt{c^2k^2 + \frac{\hbar^2k^4}{4m^2}}, \tag{4.39}$$

where $c = \sqrt{\mu/m}$ is the sound speed.

4.3 Fluid dynamics interpretation

The previous section has shown that the condensate may contain fluid structures such as waves and vortices. In this section we show the deep link between the GP equation and fluid dynamics. If we substitute the expression

$$\psi = Re^{i\theta}, \tag{4.40}$$

(where R and θ are respectively the amplitude and the phase of ψ) into Eq. (4.31), we obtain the classical continuity equation

$$\frac{\partial \rho_s}{\partial t} + \nabla \cdot (\rho_s \mathbf{v}_s) = 0, \tag{4.41}$$

which expresses conservation of mass, and the (quasi) Euler equation

$$\rho_s \left(\frac{\partial v_{sj}}{\partial t} + v_{sk}\frac{\partial v_{sj}}{\partial x_k} \right) = -\frac{\partial p}{\partial x_j} + \frac{\partial \Sigma_{jk}}{\partial x_k}, \tag{4.42}$$

where the usual convention applies of summation over repeated indices; in these expressions we have introduced the fluid's density

$$\rho_s = mR^2 = m|\psi|^2 = mn, \tag{4.43}$$

the velocity

$$\mathbf{v}_s = \frac{\hbar}{m}\nabla\theta, \tag{4.44}$$

where v_{sk}, $k = 1, 2, 3$ are the Cartesian components of $\mathbf{v}_s$. We attach the subscript s to the velocity because we think of the condensate as a pure superfluid (in the case of He II this identification is not correct: because of the strong interaction, only a fraction of the superfluid is the actual condensate; hereafter we shall ignore this difference).
In writing Eq. 4.42 we have also identified the fluid's pressure

$$p = \frac{V_0}{2m^2}\rho_s^2, \tag{4.45}$$

and a quantity called the quantum stress

$$\Sigma_{jk} = \left(\frac{\hbar}{2m}\right)^2 \rho_s \frac{\partial^2 \ln \rho_s}{\partial x_j \partial x_k}. \tag{4.46}$$

Note that, without the quantum stress, the GP equation describes a classical inviscid Euler fluid.

Chapter 5

Helium II

5.1 Thermal and mechanical effects

Early experiments showed that the motion of helium II has unusual properties. For example, consider a vessel A which contains helium and is linked to the helium in the bath B via a superleak S, as in Figure 5.1(left). A superleak is a very small hole (or holes); it can be realized, for example, by filling a channel with very fine powder, so fine that any ordinary fluid could not go through it. It was found that heating the helium in A with a resistor induces not only a temperature difference $\Delta T = T_A - T_B$, but also a flow from B to A through the superleak S, hence a pressure difference Δp, which is proportional to the height difference between the liquid in A and the liquid in B. This pressure difference can be large enough to create a small fountain, if A is open at the top (fountain effect). Note that the velocity (into A) opposes the flow of entropy (out of A), unlike what happens in an ordinary fluid.

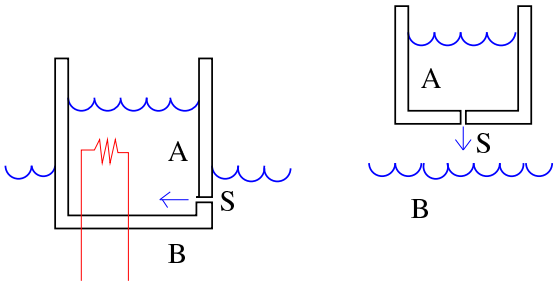

Figure 5.1: Left: thermo–mechanical effect. Right: mechano–thermal effect.

A second unusual effect, discovered by Daunt and Mendelsson and shown in Figure 5.1(right), is the following. If the vessel A is lifted above the bath B and helium flows out of the superleak S, the temperature in A increases,

whereas the temperature is B decreases. This phenomenon is called the mechano–caloric effect.

Careful measurements by Kapitza of the chemical potential μ revealed that in these experiments μ remains the same in A and B: $\mu(p_A, T_A) = \mu(p_B, T_B)$. Since $d\mu = -sdT + dp/\rho$, where s is the specific entropy, we conclude that

$$\Delta p = \rho s \Delta T, \tag{5.1}$$

In another set of experiments it was found if the temperature is reduced from He I to He II, helium's viscosity η seems to change abruptly at $T < T_\lambda$, depending on how it is measured.

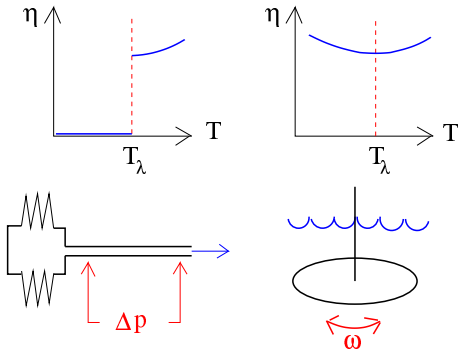

Figure 5.2: Left: the viscosity η, determined from the measurement of the pressure drop in a thin pipe, is discontinuous when plotted versus the temperature T. Right: if η is determined from the damping of an oscillating disk, it is continuous with T.

If the viscosity is measured by pushing helium along a thin capillary using bellows and detecting the pressure gradient along the capillary, then it is found that $\eta = 0$ within experimental accuracy (see Figure 5.2 left). If the viscosity is measured by observing the damping of an oscillating disk, then it is found that $\eta \neq 0$ (see Figure 5.2 right).

5.2 Landau's equations

The apparently paradoxical results described in the previous subsection are explained by the Two-Fluid model of Landau and Tisza. In this model, helium II is described as the intimate mixture of two fluids: the superfluid and the normal fluid. The first is related to the quantum ground state, and has zero viscosity and entropy. The second consists of thermal excitations and

carries the total viscosity and entropy of the liquid. Each fluid has its own velocity and density fields, $\mathbf{v}_s$ and ρ_s for the superfluid and $\mathbf{v}_n$ and ρ_n for the normal fluid; the total density of helium II, $\rho = \rho_n + \rho_s$, is approximately temperature independent. The table below summarises the Two–Fluid model:

component	velocity	density	viscosity	entropy
normal fluid	$\mathbf{v}_n$	ρ_n	η	s
superfluid	$\mathbf{v}_s$	ρ_s	0	0

The Two–Fluid model accounts for all experimental observations (at least at small velocities). The superleak S is so small that the viscous normal fluid cannot move through it: only the superfluid flows through S. The observation that the chemical potential is constant across S both in the steady state (when $\mathbf{v}_s = 0$ in the superleak) and during transients (when $\mathbf{v}_s \neq 0$) led Landau to postulate that gradients of the chemical potential are responsible for the acceleration of the superfluid.

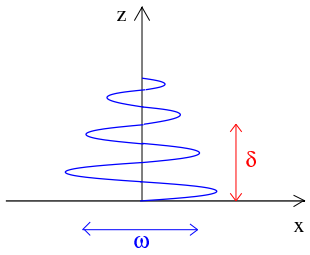

Figure 5.3: Penetration depth.

The relative proportion of superfluid and normal fluid at a given temperature was determined by Adronikashvili. He used the fact that the motion of an oscillating boundary penetrates into a viscous fluid only a distance of the order of $\sqrt{2\nu/\omega}$, where $\nu = \eta/\rho$, ν is the kinematic viscosity, η the viscosity, and ω the angular frequency of the oscillation - see Figure 5.3.

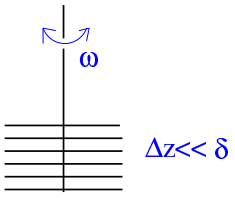

Figure 5.4: Adronikashvili's pendulum.

Adronikashvili's apparatus, shown schematically in Figure 5.4, was a special pendulum which consisted of a suspended stack of disks. Let Δz be the distance between the disks. If $\Delta z \ll \delta = \sqrt{2\eta/(\rho_n \omega)}$ the normal fluid is trapped between the disks and contributes to the moment of inertia of the pendulum, whereas the superfluid does not contribute (being inviscid, it moves freely between the disks). By measuring the damping rate of the torsional oscillations, Adronikashvili determined the ratios ρ_s/ρ and ρ_n/ρ as functions of the temperature T, which are shown schematically in Figure 5.5. Note that if the temperature is reduced the normal fluid fraction ρ_n/ρ decreases rapidly; below $T \approx 0.7$ K the normal fluid can be neglected. Note also that the rapid decrease of the superfluid fraction vs temperature is similar to the decrease of the condensate's density.

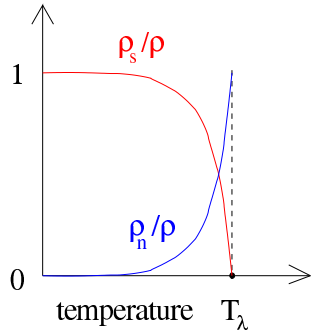

Figure 5.5:

The mathematical formulation of the Two–Fluid model consists of the equations of mass and entrophy conservation, and the equations of momentum conservation of the normal fluid and the superfluid, respectively. These equations are

$$\frac{\partial \rho}{\partial t} + \nabla \cdot (\rho_n \mathbf{v}_n + \rho_s \mathbf{v}_s) = 0, \tag{5.2}$$

$$\frac{\partial (\rho s)}{\partial t} + \nabla \cdot (\rho s \mathbf{v}_n) = 0, \tag{5.3}$$

$$\frac{\partial \mathbf{v}_n}{\partial t} + (\mathbf{v}_n \cdot \nabla)\mathbf{v}_n = -\frac{1}{\rho}\nabla p - \frac{\rho_s}{\rho_n} s \nabla T + \frac{\eta}{\rho_n}\nabla^2 \mathbf{v}_n, \tag{5.4}$$

$$\frac{\partial \mathbf{v}_s}{\partial t} + (\mathbf{v}_s \cdot \nabla)\mathbf{v}_s = -\frac{1}{\rho}\nabla p + s \nabla T. \tag{5.5}$$

Equation 5.3 states that entropy flows with the normal fluid. In isothermal conditions, the superfluid obeys the classical Euler equation, and the normal fluid obeys the classical Navier–Stokes equation.

Finally Landau recognised that, since $\mathbf{v}_s$ is proportional to the gradient of the phase of a quantum mechanical wavefunction, we must also have

$$\nabla \times \mathbf{v}_s = 0. \tag{5.6}$$

It must be stressed that Equation (5.4) and (5.5) are valid only at small velocities. In the presence of quantised vortices Landau's equation require modifications.

5.3 Second sound

The existence of two separate fluid components has a striking consequence on the oscillatory motion of helium II. Let us consider helium at rest ($\mathbf{v}_{n0} = 0$, $\mathbf{v}_{s0} = 0$) with density $\rho_0 = \rho_{s0} + \rho_{n0}$, pressure p_0, temperature T_0 and entropy s_0. We introduce small perturbations (indicated by primed quantities) $\rho = \rho_0 + \rho'$, $\rho_n = \rho_{n0} + \rho'_n$, $\rho_s = \rho_{s0} + \rho_s$, $\mathbf{v}_n = \mathbf{v}'_n$, $\mathbf{v}_s = \mathbf{v}'_s$, $p = p_0 + p'$, $T = T_0 + T'$ and $s = s_0 + s'$; neglecting quadratic terms in the perturbations, Landau's equations become

$$\frac{\partial \rho'}{\partial t} + \rho_{n0} \nabla \cdot \mathbf{v}'_n + \rho_{s0} \nabla \cdot \mathbf{v}'_s = 0, \tag{5.7}$$

$$\rho_0 \frac{\partial s'}{\partial t} + s_0 \frac{\partial \rho'}{\partial t} + \rho_0 s_0 \nabla \cdot \mathbf{v}'_n = 0, \tag{5.8}$$

$$\frac{\partial \mathbf{v}'_n}{\partial t} = -\frac{1}{\rho_0} \nabla p' - \frac{\rho_{s0}}{\rho_{n0}} s_0 \nabla T', \tag{5.9}$$

$$\frac{\partial \mathbf{v}'_s}{\partial t} = -\frac{1}{\rho_0} \nabla p' + \rho_{s0} s_0 \nabla T'. \tag{5.10}$$

In writing these equations we have neglected the viscous term $\eta \nabla^2 v_{\mathrm{n}}$, because we know already that its effect is simply to damp any motion. Assuming solution of the form $e^{i\omega(t - x/c)}$, we find two values for the phase speed c:

$$c_1 = \sqrt{\left(\frac{\partial p}{\partial \rho}\right)_0}, \tag{5.11}$$

$$c_2 = \sqrt{\frac{\rho_{s0} s_0^2 T_0}{\rho_{n0} C_V}}. \tag{5.12}$$

We conclude that there are two modes of oscillation. The first mode is a pressure and density wave at (almost) constant temperature and entropy,

in which $\mathbf{v}_n$ and $\mathbf{v}_s$ move in phase. In analogy with ordinary sound, we call this mode *first sound*. The second mode is a temperature and entropy wave at (almost) constant pressure and density, in which $\mathbf{v}_n$ and $\mathbf{v}_s$ move in anti–phase. We call this mode *second sound*. The speed of first sound is $c_1 \approx 200$ m/s at all temperatures; the speed of second sound, c_2, is approximately ten times less, and drops to zero as $T \to T_\lambda$.

It is interesting to notice that, in the case of second sound, temperature perturbations obey the wave equation

$$\frac{\partial^2 T'}{\partial t^2} \approx c_2^2 \nabla^2 T',$$

whereas in ordinary fluids (e.g. helium I) temperature perturbations obey the heat equation

$$\frac{\partial T'}{\partial t} = \kappa \nabla^2 T'.$$

5.4 Thermal counterflow

Another consequence of the Two Fluid model is the unusual form of heat transfer. Consider Figure 5.6. A closed channel is open to the helium bath at one end. A resistor, placed at the closed end, dissipates a known heat flux $\dot{Q}$. This heat flux is carried away by the normal fluid, $v_n = \dot{Q}/(\rho S T)$. With the channel being closed, the mass flux is zero, $\rho_n v_n + \rho_s v_s = 0$, hence the superfluid moves towards the resistor, $v_s = (\rho_n/\rho_s) v_n$, setting up a counterflow velocity $v_{ns} = v_n - v_s$ which is proportional to the applied heat flux:

$$v_{ns} = v_n - v_s = \frac{\dot{Q}}{\rho_s S T}. \tag{5.13}$$

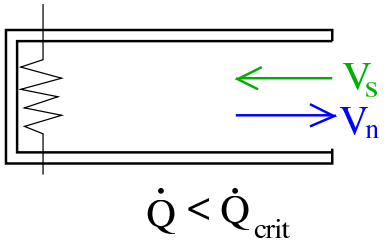

Figure 5.6: Laminar counterflow for $\dot{Q} < \dot{Q}_{crit}$.

Provided that $\dot{Q}$ is less than a critical heat flux $\dot{Q}_c$, this form of heat transfer is laminar. We shall see that at high heat flux the counterflow becomes turbulent.

Chapter 6

Critical velocity

6.1 Helium II

The normal fluid consists of thermal excitations of energy ϵ and momentum $\mathbf{p}$. Landau showed that the shape of the dispersion curve $\epsilon = \epsilon(p)$, where $p = |\mathbf{p}|$, is responsible for the superfluid nature of helium II. Landau's spectrum, confirmed by neutron scattering experiments, is shown in Figure 6.1. Note the minimum at momentum p_0 and energy Δ. The excitations at low p (linear part of the spectrum) are called *phonons*; the excitations in the quadratic region near the minimum of the dispersion curve are called *rotons*.

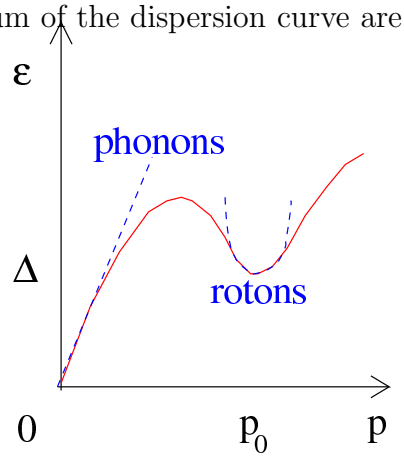

Figure 6.1: Landau's spectrum of the excitations. Note the roton minimum at (p_0, Δ_0).

Landau's argument for superfluidity is the following. Consider an object which moves in He II, for example a negative ion, which carves a little bubble of radius $\approx 12 \times 10^{-8}$cm and mass $\approx 100 m_{He}$. The object has mass m

and moves with velocity V_1, momentum $\mathbf{p}_1 = mV_1$ and energy E_1; the object creates an excitation of energy ϵ and momentum $\mathbf{p}$, changing its own energy and momentum to E_2 and $\mathbf{p}_2$. Conservation of energy and momentum requires $E_1 = E_2 + \epsilon$ and $\mathbf{p}_1 = \mathbf{p}_2 + \mathbf{p}$, hence

$$P_1 p \cos\theta = m\epsilon + \frac{1}{2}p^2, \tag{6.1}$$

where θ is the angle between $\mathbf{p}_1$ and $\mathbf{p}$. Thus the object can lose energy and create an excitation if the initial velocity satisfies

$$V_1 > \frac{p}{2m} + \frac{\epsilon}{p} \approx \frac{\epsilon}{p}. \tag{6.2}$$

Let us minimise this velocity ϵ/p:

$$\frac{d}{dp}\left(\frac{\epsilon}{p}\right) = -\frac{1}{p^2}\epsilon + \frac{1}{p}\frac{d\epsilon}{dp} = 0. \tag{6.3}$$

We find:

$$\frac{d\epsilon}{dp} = \frac{\epsilon}{p}. \tag{6.4}$$

The minimum of ϵ/p thus corresponds to the line from the origin to a point slightly to the right of (p_0, Δ) on the dispersion curve; the critical velocity is $V_1 = V_c = 58$ m/s (at SVP). In conclusion, at sufficiently low temperature such that the normal fluid is negligible, we expect the ion to experience no drag for $0 < V_1 < V_c$.

At SVP, an ion moving in liquid helium creates a vortex ring at velocity smaller than V_c. Fortunately, at higher pressures the velocity of roton creation is smaller than the velocity required to create a vortex ring, and Landau's argument can be tested directly, as done by McClintock and collaborators. Fig. 6.2 shows the measured drag as a function of the ion's velocity. The striking result is that at $T = 0.35$ K, in helium II, the drag is zero for $V_1 < V_c$ within experimental accuracy. The second curve at the left of the figure shows the drag measured at $T = 4$ K, in helium I, which is a classical fluid. This experiment is thus a direct observation of superfluid behaviour.

6.2 BEC and ideal gas

In the case of a Bose–Einstein condensate, we have seen that the dispersion relation is

$$\omega = \sqrt{c^2k^2 + \frac{\hbar^2k^4}{4m^2}}, \tag{6.5}$$

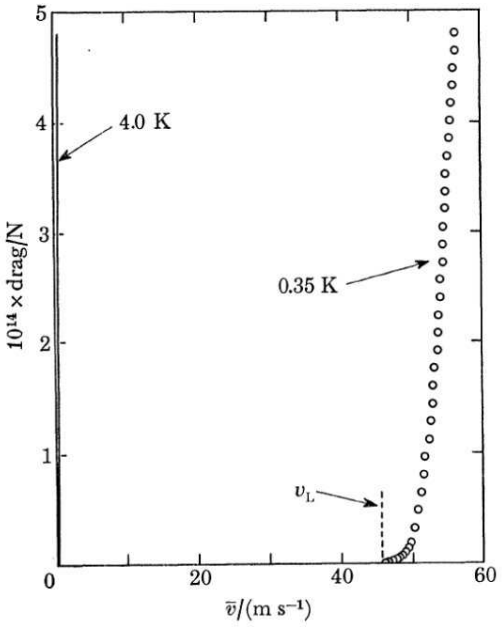

Figure 6.2: Measured drag in helium I (left curve) and helium II (right curve). Note that in He II there is no drag (superfluidity) for $V < V_c$.

Since $\epsilon = \hbar\omega$ and $p = \hbar k$, we can rewrite this expression as

$$\epsilon = \sqrt{c^2p^2 + \frac{\hbar^2 p^4}{4m^2}} \approx cp \text{ for } p << 1, \tag{6.6}$$

Thus for small p we have $\epsilon/p \approx c$ and Landau's argument applies: an object which moves at velocity larger than $\epsilon/p = c$ creates a sound wave (phonon) and loses energy. An object which moves at velocity less than c cannot lose energy, hence the BEC is a superfluid.

Finally, let us consider the case of a classical ideal gas. In this case the dispersion relation is given by $\epsilon = v^2/(2m)$ where $p = mv$, hence

$$\epsilon = \frac{p^2}{2m}, \tag{6.7}$$

This means that the minimum of ϵ/p occurs at $p = 0$. We conclude that an ideal gas is not a superfluid, because an object moving at any nonzero velocity in the gas loses energy.

Chapter 7

Quantised vortex lines

7.1 Helium in rotation

Quantum mechanics introduces remarkable constraints on the rotational motion of helium II. It is instructive to consider the rotation of an ordinary, classical fluid first. A bucket of water which rotates at constant angular velocity Ω around the z axis has a height profile given by

$$z = \frac{\Omega^2 r^2}{2g}, \tag{7.1}$$

as shown in Figure 7.1 left; the water's velocity field is $\mathbf{v} = \Omega\hat{\phi}$ (solid body rotation), and the vorticity is $\boldsymbol{\omega} = \nabla \times \mathbf{v} = 2\Omega\hat{\mathbf{z}}$, where $\hat{\mathbf{z}}$ and $\hat{\phi}$ are the unit vectors along the axial and azimuthal direction respectively.

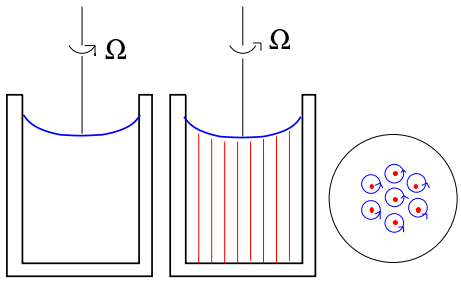

Figure 7.1: Left: classical fluid in rotation. Middle: rotating helium II. Right: top view of the vortex lattice.

The rotation of helium II is very different, because quantum mechanics introduces important constraints on the rotational motion. According to the two–fluid model, $\nabla \times \mathbf{v}_s = 0$, which means that the superfluid component cannot rotate; we expect that the profile of rotating helium II is

$$z = \left(\frac{\rho_n}{\rho}\right)\frac{\Omega^2 r^2}{2g}. \tag{7.2}$$

which is temperature dependent.

The observed profile did not agree with this prediction. The puzzle was solved by Onsager (1949) and Feynmanni (1955), who argued that the superfluid forms vortex lines (as in Figure 7.1, middle and right) around which the circulation κ is quantised:

$$\oint_C \mathbf{v}_s \cdot \mathbf{d}\boldsymbol{\ell} = \kappa, \tag{7.3}$$

where $h = 6.626 \times 10^{-27}$ergs is Planck's constant. The quantum of circulation in helium II (measured by Vinen in 1961) is

$$\kappa = \frac{h}{m} = 9.97 \times 10^{-4} \text{ cm}^2 \text{ s}^{-1}, \tag{7.4}$$

where $m = 6.648 \times 10^{-24}$g is the mass of the helium atom.

Figure 7.2: Vortex line

.

Equation 7.3 can be used to determine the velocity field $\mathbf{v}_\text{s}$. Let C be a circle of radius r around the axis of the vortex; using cylindrical coordinates r, ϕ, z, the ϕ component of the superfluid velocity is

$$v_s = \frac{\kappa}{2\pi r}, \tag{7.5}$$

as shown in Figure 7.3.

Since the vortex core is hollow, Equation 7.5 is valid only for $r \geq a_0$ where $a_0 \approx 10^{-8}$ is the vortex core radius.

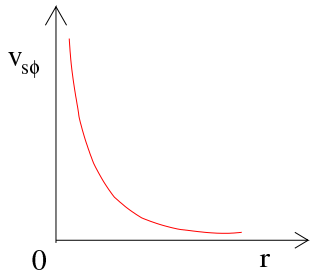

Figure 7.3: Velocity field around a vortex line.

7.2 The first vortex

The critical angular velocity Ω_c for the appearance of the first vortex line can be determined in the following way. Thermodynamical equilibrium requires minimisation of the free energy, $F = E - TS$ in the rotating frame of reference, which is

$$F' = F - \mathbf{\Omega} \cdot \mathbf{L} = E - TS - \mathbf{\Omega} \cdot \mathbf{L}, \tag{7.6}$$

where E is internal energy, $\mathbf{\Omega}$ the angular velocity, and $\mathbf{L}$ the angular momentum. Let $T = 0$ and consider helium II contained in a rotating cylinder of radius R. The first vortex appears if

$$\Delta F' = F'_{vortex} - F'_{no\ vortex} = E - \Omega L < 0, \tag{7.7}$$

where the energy and the angular momentum (per unit length) are

$$E = \int_0^{2\pi} d\phi \int_{a_0}^{R} \frac{\rho_s v_s^2}{2} r dr, \tag{7.8}$$

$$L = \int_0^{2\pi} d\phi \int_{a_0}^{R} \rho_s r v_s r dr. \tag{7.9}$$

Substituting $v_s = \kappa/(2\pi r)$ we find that the critical velocity of vortex appearance is

$$\Omega_c = \frac{\kappa}{2\pi R^2} \ln (R/a_0), \tag{7.10}$$

where $a_0 \approx 10^{-8}$ cm is the vortex core radius.

7.3 Vortex lattice

If Ω is increased past Ω_c, more and more vortex lines appear in the flow. A bucket of helium rotating at constant angular velocity $\Omega > \Omega_c$ contains a

lattice of quantised vortex lines aligned along the axis of rotation as shown in Figure 7.1. The lattice is steady in the rotating frame (see Figure 7.1 right; the number of vortex lines per unit area is given by Feynman's rule

$$n = \frac{2\Omega}{\kappa}. \tag{7.11}$$

Note that although the microscopic superflow is potential ($v_s \sim 1/r$), the macroscopically–averaged flow which results from the vortex lattice corresponds to solid body rotation ($v_s \sim \Omega r$). In other words, by creating n quantised vortices per unit area, helium II has the same (large–scale) vorticity of a classical rotating fluid ($2\Omega = n\kappa$).

Equation (7.11) has been tested by direct visualisation of quantised vortices at low temperatures by Williams and Packard (1974); their technique consisted in trapping electrons along the vortex lines and then collecting them on electrodes at the top of the container. Fig. /reffig:packard shows vortex lattices at increasing rotation rates Ω. More recently, direct visualisation of quantised vorticity by tracer particles imaged by a laser (Fig. 7.5 was achieved by Bewley *et al.* (2006) and by Zhang and Van Sciver (2005). Quantised vorticity in atomic Bose–Einstein condensates (Fig. 7.6) has also been observed directly using lasers (Madison *et al.* 2000) by various groups.

7.4 Mutual friction

Quantised vortex lines interact with the phonons and rotons which make up the normal fluid of helium II, thus coupling the superfluid component with the normal fluid component (Barenghi, Donnelly and Vinen 1983). The coupling force $\mathbf{F}_{ns}$, called *mutual friction*, is proportional to the relative velocity between the two fluids, and acts as a friction on each fluid. Thus, in the presence of quantised vorticity, the governing equations of the Two–Fluid model become

$$\rho_n \left(\frac{\partial \mathbf{v}_n}{\partial t} + (\mathbf{v}_n \cdot \nabla)\mathbf{v}_n \right) = -\frac{\rho_n}{\rho}\nabla p - \rho_s s \nabla T, + \eta \nabla^2 \mathbf{v}_n + \mathbf{F}_{ns}, \tag{7.12}$$

$$\rho_s \left(\frac{\partial \mathbf{v}_s}{\partial t} + (\mathbf{v}_s \cdot \nabla)\mathbf{v}_s \right) = -\frac{\rho_s}{\rho}\nabla p + \rho_s s \nabla T - \mathbf{F}_{ns}. \tag{7.13}$$

The precise form of the friction depends whether the vortex lines form a disordered tangle or are aligned (by the rotation for example).

Consider a vessel which contains helium II and rotates at constant angular velocity Ω. A second sound pulse or resonance which moves across helium

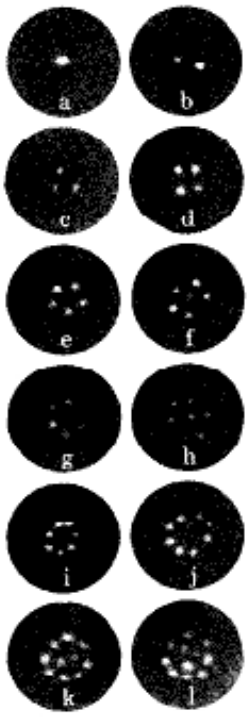

Figure 7.4: The first direct visualization of quantised vortices by Packard's group at UC Berkely. What is shown are vortex lattices at increasing values of Ω.

Figure 7.5: Micron-size solid hydrogen particles trapped in a vortex lattice in superfluid helium, as observed by Bewley *et al.* (2006).

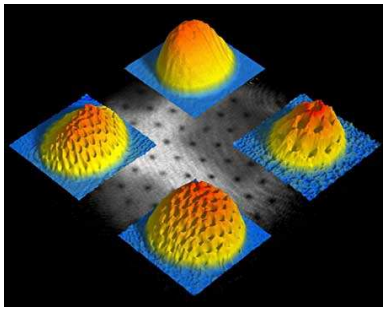

Figure 7.6: Vortex lattices in Bose–Einstein condensates at different values of the rotation rate Ω observed by Ketterle's group at MIT. What is shown is the density profiles; vortices correspond to holes.

suffers a bulk attenuation. What concerns us here is the extra attenuation which arises due to the presence of vortices, shown in Figure 7.7. This extra attenuation can be used to measure the density of vortex lines.

Hall and Vinen (1956) showed that the mutual friction force is

$$\mathbf{F}_{ns} = \frac{B\rho_n\rho_s}{\rho}\hat{\mathbf{\Omega}} \times (\mathbf{\Omega} \times \mathbf{q}) + \frac{B'\rho_n\rho_s}{\rho}\mathbf{\Omega} \times \mathbf{q}, \tag{7.14}$$

where

$$\mathbf{q} = \mathbf{v}_n - \mathbf{v}_s, \tag{7.15}$$

and B and B' are dimensionless temperature–dependent mutual friction coefficients which depend on the interaction of phonons and rotons with the quantised vortices. Substituting $\mathbf{q}$ and $\mathbf{F}$ into the Equation (7.12) and Equation (7.13), we obtain the following second sound wave equation:

$$\frac{d^2\mathbf{q}}{dt^2} + (2 - B')\mathbf{\Omega} \times \frac{d\mathbf{q}}{dt} - B\hat{\mathbf{\Omega}} \times (\mathbf{\Omega} \times \frac{d}{dt}\mathbf{q}) = c_2^2\nabla(\nabla \cdot \mathbf{q}) \tag{7.16}$$

Let us assume that the second sound propagates in the x direction:

$$\mathbf{q} = (q_x, q_y, 0)e^{ikx - i\omega t}, \tag{7.17}$$

where k is the wavenumber and ω the angular frequency. In typical experimental conditions we have $\Omega/\omega \ll 1$, hence we obtain

$$k \approx \frac{1}{c_2}(\omega + i\frac{\Omega B}{2}). \tag{7.18}$$

The attenuation coefficient $\tilde{\alpha}$ is the imaginary part of k:

$$\tilde{\alpha} = \frac{B\Omega}{2c_2}. \tag{7.19}$$

In fact

$$\mathbf{q} = (q_x, q_y, 0)e^{-\tilde{\alpha}x}e^{i\omega(x/c_2 - t)}, \tag{7.20}$$

Note that angular velocity of rotation Ω is related to the vortex line density L via Feynman's rule, Equation (7.11), so, by measuring $\tilde{\alpha}$, we can recover the vortex line density.

It is therefore possible to perform an absolute measurement of the amount of vortex lines which are present in a turbulent flow. First the vessel is rotated, and the second sound signal is calibrated against the known vortex line density (number of vortices per unit area) $L = 2\Omega/\kappa$. Secondly, the vessel is stopped, the turbulence experiment is performed, and the second sound attenuation allows us to recover the vortex line density L (now to be interpreted as the vortex length per unit volume). Finally, it must be noticed that second sound is not attenuated by vortex lines which are parallel to the direction of propagation. If we assume that the turbulence is isotropic, only 2/3 of the vortices will attenuate the second sound wave.

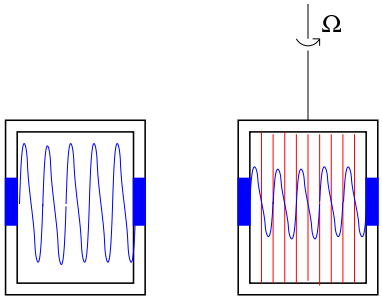

Figure 7.7: Left: second sound wave in a non–rotating vessel (no vortices). Right: second sound wave in the presence of vortices in a rotating vessel (vortices are present): note the reduced amplitude of the wave.

7.5 Vortex dynamics

7.5.1 The Biot–Savart law

In helium II the radius of the vortex core, approximately $a \approx 10^{-8}$ cm, is much smaller than any length scale of interest (for example, the typical distance between vortex lines), so it is a good idea to approximate vortex

lines as space curves of infinitesimal thickness. This approach was introduced by Schwarz. The curves must be either closed loops or end at a boundary because a vortex cannot terminate in the middle of the flow.

Let $\mathbf{s} = \mathbf{s}(\xi)$ be the position of a point on such a curve, where ξ is the arc length. Following the classical theory of space–curves, we define the tangent $\hat{\mathbf{T}}$, normal $\hat{\mathbf{N}}$ and binormal $\hat{\mathbf{B}}$ unit vectors:

$$\mathbf{s}' = \frac{d\mathbf{s}}{d\xi} = \hat{\mathbf{T}}, \tag{7.21}$$

$$\frac{d\hat{\mathbf{T}}}{d\xi} = c\hat{\mathbf{N}}, \tag{7.22}$$

$$\hat{\mathbf{B}} = \hat{\mathbf{T}} \times \hat{\mathbf{N}}, \tag{7.23}$$

where $c = |\mathbf{s}''|$ is the curvature and $R = 1/c$ the local radius of curvature. The three vectors $\hat{\mathbf{T}}$, $\hat{\mathbf{N}}$ and $\hat{\mathbf{B}}$ form a right–handed system, as shown in Figure 7.8.

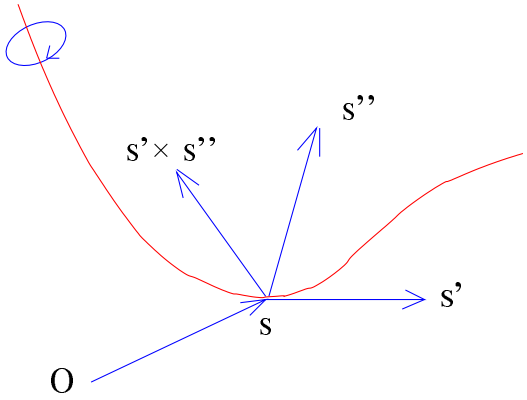

Figure 7.8: Tangent, normal and binormal vectors.

The next step is to find the equation of motion of the vortex line. We start from classical definition of vorticity field $\boldsymbol{\omega}$ associated with a velocity field $\mathbf{v}$:

$$\boldsymbol{\omega} = \nabla \times \mathbf{v}. \tag{7.24}$$

Let us introduce the vector potential $\mathbf{v} = \nabla \times \mathbf{A}$; then $\mathbf{A}$ obeys the Poisson equation

$$\nabla^2 \mathbf{A} = -\boldsymbol{\omega}, \tag{7.25}$$

whose solution is

$$\mathbf{A}(\mathbf{x}) = \frac{1}{4\pi} \int \frac{\boldsymbol{\omega}(\mathbf{x}')d^3x'}{r}, \tag{7.26}$$

where $r = |\mathbf{x} - \mathbf{x}'|$. In our case the vorticity is formally concentrated on the vortex filament, $\boldsymbol{\omega}(\mathbf{x}')d^3x' = \kappa \mathbf{d}\boldsymbol{\ell}(\mathbf{x}')$, thus

$$\mathbf{A} = \frac{\kappa}{4\pi} \oint \frac{1}{r} \mathbf{d}\boldsymbol{\ell}', \tag{7.27}$$

from which we obtain the Biot–Savart law

$$\mathbf{v}(\mathbf{x}) = -\frac{\kappa}{4\pi} \oint \frac{(\mathbf{x} - \mathbf{x}')}{r^3} \times \mathbf{d}\boldsymbol{\ell}'. \tag{7.28}$$

The Biot–Savart law is often too difficult for analytical purpose, and is also computationally expensive. In many cases it is convenient to replace it with the following Local Induction Approximation (LIA):

$$\mathbf{v}(\mathbf{x}) \approx \beta \mathbf{s}' \times \mathbf{s}'', \tag{7.29}$$

where

$$\beta = \frac{\kappa}{4\pi R} \ln (R/a_{eff}), \tag{7.30}$$

where a_{eff} is an effective core radius and $R = 1/|\mathbf{s}''|$. It is apparent from the LIA that a vortex filament at a given position moves in the binormal direction with speed which is inversally proportional to radius of curvature at that position.

7.5.2 The Schwarz equation

Now we take into account friction. Let $\mathbf{v}_L$ be the vortex line velocity. The forces acting on unit length of vortex line are the Magnus force $\mathbf{f}_M$ and the drag force $\mathbf{f}_D$:

$$\mathbf{f}_M = \rho_s \boldsymbol{\kappa} \times (\mathbf{v}_L - \mathbf{v}_s), \tag{7.31}$$

$$\mathbf{f}_D = \rho_s \kappa \alpha \mathbf{s}' \times [\mathbf{s}' \times (\mathbf{v}_s - \mathbf{v}_n)] + \alpha' \mathbf{s}' \times (\mathbf{v}_s - \mathbf{v}_n), \tag{7.32}$$

where $\boldsymbol{\kappa} = \kappa \mathbf{s}' = \kappa \hat{\boldsymbol{\omega}}$. Both $\mathbf{f}_M$ and $\mathbf{f}_D$ are forces per unit length of vortex line. The Magnus force arises in general when there is a flow past a body

with circulation (in this case the vortex core); on one side of the body the flow is faster, hence the pressure is lower, which causes a transverse force, see Figure 7.9.

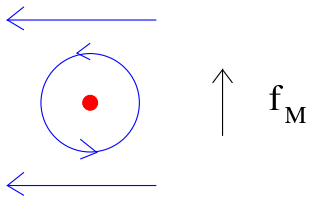

Figure 7.9: Magnus force.

The drag force consists of a parallel and transverse part, and is parametrised by friction coefficients α and α' which are related to the mutual friction coefficients B and B' already introduced by

$$\alpha = \frac{B\rho_n}{2\rho}, \qquad \alpha' = \frac{B'\rho_n}{2\rho}. \tag{7.33}$$

Since the vortex core is very small, it has approximately no inertia, thus $\mathbf{f}_M + \mathbf{f}_D = \mathbf{0}$. We obtain Schwarz's equation (Schwarz 1988)

$$\mathbf{v}_L = \frac{d\mathbf{s}}{dt} = \mathbf{v}_s - \alpha\mathbf{s}' \times (\mathbf{v}_s - \mathbf{v}_n) + \alpha'\mathbf{s}' \times [\mathbf{s}' \times (\mathbf{v}_s - \mathbf{v}_n)], \tag{7.34}$$

where we decompose

$$\mathbf{v}_s = \mathbf{v}_s^{self} + \mathbf{v}_s^{ext}. \tag{7.35}$$

Here $\mathbf{v}_s^{self}$ is the self–induced velocity (Biot–Savart or LIA) and $\mathbf{v}_s^{ext}$ is an externally applied superflow.

Under LIA, we have $\mathbf{v}_s^{self} = \beta\mathbf{s}' \times \mathbf{s}''$ and Schwarz's equation reduces to

$$\begin{aligned}\frac{d\mathbf{s}}{dt} = \mathbf{v}_s^{ext} + \beta\mathbf{s}' \times \mathbf{s}'' + \alpha\mathbf{s}' \times (\mathbf{v}_{ns}^{ext} - \beta\mathbf{s}' \times \mathbf{s}'') \\ -\alpha'\mathbf{s}' \times [\mathbf{s}' \times (\mathbf{v}_{ns}^{ext} - \beta\mathbf{s}' \times \mathbf{s}'')],\end{aligned}$$

where $\mathbf{v}_{ns}^{ext} = \mathbf{v}_n^{ext} - \mathbf{v}_s^{ext}$

The numerical method to move vortex filaments (Schwarz 1988) consists in dividing each filament into a large number of vortex points; each vortex points moves according to Schwarz's equation.

7.5.3 Kelvin waves

Consider a vortex line which is straight and aligned in the z direction. Let $\mathbf{s} = \mathbf{s}(\xi)$ be the position of a point along the line. We use the LIA, Equation (7.29), to determine the self–induced motion of the vortex. Clearly if the vortex is straight, then $\mathbf{s}'' = 0$ and $\mathbf{v}_s^{self} = \beta \mathbf{s}' \times \mathbf{s}'' = 0$, that is to say the vortex does not move.

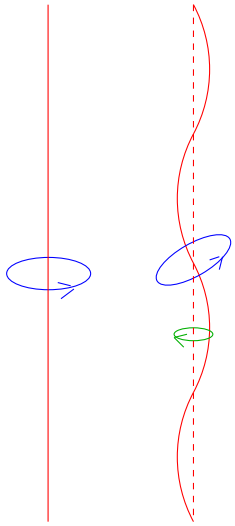

Figure 7.10: Kelvin wave on a vortex line.

Now suppose that the vortex line is slightly perturbed away from the straight position in the form of a helix as in Figure 7.10:

$$\mathbf{s} = (\epsilon \cos\phi, \epsilon \sin\phi, z), \tag{7.36}$$

where $\phi = kz - \omega t$, ϵ is the amplitude of the helical wave, and ω_0 is the angular frequency. If $\epsilon \ll 1$ then $z \approx \xi$. We have $\mathbf{s}' = (-k\epsilon \sin\phi, k\epsilon \cos\phi, 1)$, $\mathbf{s}'' = (-k^2\epsilon \cos\phi, -k^2\epsilon \sin\phi, 0)$ and, neglecting terms proportional to ϵ^2, we conclude that the amplitude ϵ is constant and that the angular frequency is

$$\omega = \omega_0 = \beta k^2, \tag{7.37}$$

which is the dispersion relation for Kelvin waves.

Chapter 8

Quantum turbulence

8.1 The vortex tangle

Configurations of vortex lines can be either laminar or turbulent. An example of laminar vortex configuration is the rotating vortex lattice, shown in Figure 7.1 (middle). Turbulent vortex configurations are easily created in the laboratory by applying a sufficiently large heat current, or by stirring the liquid helium using grids or propellers. ccording to numerical simulations, the resulting quantum turbulence consists of a tangle of quantised vortices, as shown in Figure 8.1.

Figure 8.1: Vortex tangle (numerical simulation).

The tangle can be characterised by the vortex line density, L, which

is defined as the length of quantised vortex lines per unit volume. From the vortex line density, a dimensional argument suggetsts that the typical separatin between the vortices is $\ell \approx L^{-1/2}$. Thus $v \approx \kappa/(2\pi\ell)$ is the typical velocity inside the tangle.

8.2 Turbulent counterflow

The study of quantum turbulence was pioneered by Vinen (1957), who generated the turbulence by the application of a heat current. This form of quantym turbulence, which has no classical analogy, is called counterflow turbulence. We have seen that heat transfer in helium II takes the form of a counter current of $\mathbf{v}_n$ and $\mathbf{v}_s$. Vinen showed that if $\dot{Q}$ (hence $V_{ns} = V_n - V_s$) exceeds a critical value $\dot{Q}_c$, then this laminar counterflow breaks down, and a tangle of vortex lines appears, see Figure 8.2.

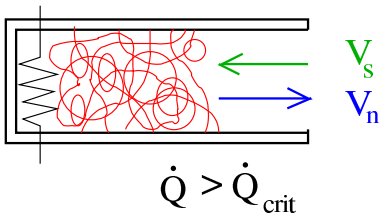

Figure 8.2: Turbulent counterflow for $\dot{Q} > \dot{Q}_{crit}$.

The vortex lines can be detected by monitoring the amplitude of a second sound signal across the channel; the measured vortex line density is

$$L = \gamma^2 V_{ns}^2, \tag{8.1}$$

where γ depends on temperature.

In the first approximation counterflow turbulence is homogeneous and the only important length scale is the intervortex distance $\delta \approx L^{-1/2}$, where L is the vortex line density. Vinen argued that L is due to the balance of production and destruction processes, which he modelled as the growth of vortex rings and the annihilation of opposite oriented vortex lines, obtaining

$$\frac{dL}{dt} = \frac{\chi_1 B \rho_n}{2\rho} V_{ns} L^{3/2} - \frac{\chi_2 \kappa}{2\pi} L^2, \tag{8.2}$$

where χ_1 and χ_2 are dimensionless constants of order one. The steady state solution to Equation (8.2) is indeed Equation (8.1) where

$$\gamma = \frac{\pi B \rho_n \chi_1}{\kappa \rho \chi_2}. \tag{8.3}$$

Tough (1987)(1987) discovered the existence of a second critical velocity, past which the vortex line density is larger. He called this second state of turbulence the T-2 state, to distinguish it from the less intense turbulent regime at smaller values of V_{ns}, called the T-1 state, see Figure 8.3.

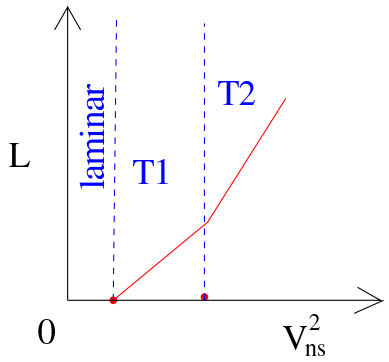

Figure 8.3: Laminar and turbulent regimesin thermal counterflow.

The natural question that arises is what is the nature of the two turbulent regimes. Melotte and Barenghi (1988) showed that the laminar normal fluid profile in a channel can become unstable at relatively small velocity if there are enough vortex lines. They considered a channel of circular cross section and radius R and a parabolic normal fluid profile of amplitude V_{ax} in the presence of the vortex line density L. Using the following model equation for the normal fluid,

$$\rho_n \left(\frac{\partial \mathbf{v}_n}{\partial t} + (\mathbf{v}_n \cdot \nabla)\mathbf{v}_n \right) = -\frac{\rho_n}{\rho}\nabla p - \rho_s S \nabla T + \eta \nabla^2 \mathbf{v}_n - \left(\frac{B\rho_n \rho_s}{2\rho} \right) \left(\frac{2}{3} \right) \kappa L (\mathbf{v}_n - \mathbf{v}_s), \tag{8.4}$$

they performed a stability analysis. which showed that the normal fluid profile becomes unstable at approximately the same critical value of L which corresponds to the observed values of the T-1 to T-2 transition. This suggests that in the T-1 state the superfluid is turbulent but the normal fluid is not, and in the T-2 state both superfluid and normal fluid are turbulent.

8.3 Vortex reconnections and turbulence

The first numerical simulations of quantum turbulence were performed by Schwarz (1988). His method consists in discretizing vortex filaments into

a large (variable) number of points, and moving each point according to Eq. 7.34, which is

$$\mathbf{v}_L = \frac{d\mathbf{s}}{dt} = \mathbf{v}_s - \alpha\mathbf{s}' \times (\mathbf{v}_s - \mathbf{v}_n) + \alpha'\mathbf{s}' \times [\mathbf{s}' \times (\mathbf{v}_s - \mathbf{v}_n)], \qquad (8.5)$$

where $\mathbf{v}_s = \mathbf{v}_s^{self} + \mathbf{v}_s^{ext}$, $\mathbf{v}_s^{ext}$ is an externally applied superflow, and $\mathbf{v}_s^{self}$ is the self–induced velocity, obtained either from the Biot–Savart integral or the LIA.

Schwarz realised that another feature is essential to understand and model the dynamics of quantum turbulence: vortex reconnections, shown schematically in Figure 8.4. His numerical algorithm performed reconnections when the distance between two vortex filaments was less then the discretization distance along each filament. Schwarz's insight was confirmed by Koplick and Levine (1993) who demonstrated the existence of vortex reconnections by directly solving the GP equation.

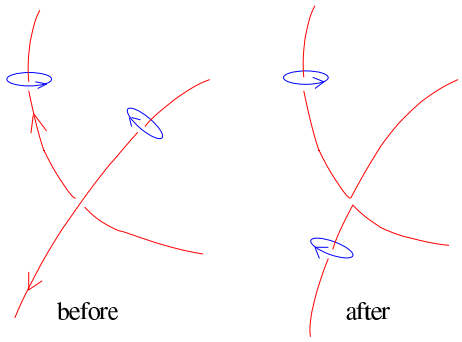

Figure 8.4: A vortex reconnection.

The typical initial condition of a numerical calculation of quantum turbulence consists of few seeding vortex rings. In the presence of a counterflow velocity V_{ns}, the rings distort each other, reconnect, more loops are created, until a random–looking vortex tangle is generated (Fig. 8.5) in which the vortex line density oscillates around a non–zero statistical steady state (Fig. 8.6).

8.3.1 The Donnelly–Glaberson instability

Besides vortex reconnections, an important ingredient for the dynamics of turbulence is the Donnelly–Glaberson instability (Cheng, Cromar and Donnelly 1973, Ostermeir and Glaberson 1975). Consider the Schwarz equation

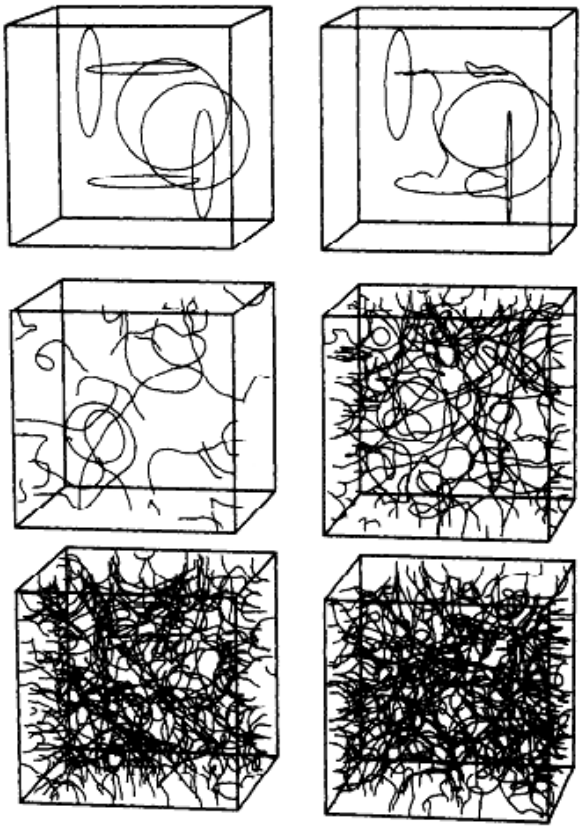

Figure 8.5: Numerical calculation of quantum turbulence starting from few vortex rings (Schwarz 1988).

$$\frac{d\mathbf{s}}{dt} = \mathbf{v}_s^{self} + \alpha \mathbf{s}' \times (\mathbf{v}_{ns}^{ext} - \mathbf{v}_s^{self}) - \alpha' \mathbf{s}' \times [\mathbf{s}' \times (\mathbf{v}_{ns} - \mathbf{v}_s^{self})]. \tag{8.6}$$

Let us assume that $\mathbf{v}_{ns} = \mathbf{v}_n - \mathbf{v}_s$ is in the direction parallel to the vortex line: $\mathbf{v}_{ns}^{ext} = (0; 0; V_{ns})$. We obtain

$$\omega = \omega_0 + \alpha'(kV_{ns} - \beta k^2), \tag{8.7}$$

and

$$\frac{d\epsilon}{dt} = \sigma\epsilon. \tag{8.8}$$

The first equation says that the friction changes the frequency of the Kelvin wave, ω_0. In the second equation $\sigma = \alpha(kV_{ns} - \beta k^2)$ is the growth rate of the Kelvin wave. The solution of Equation 8.8 is

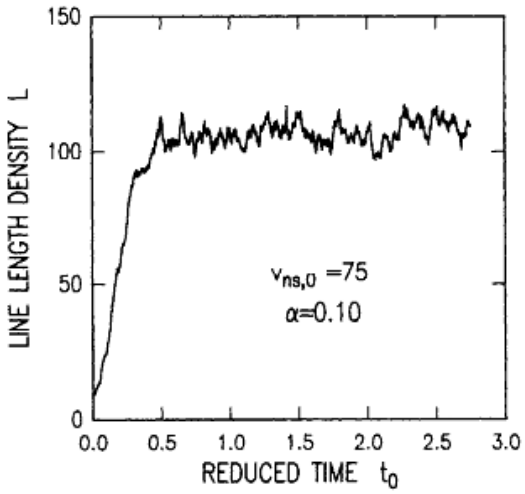

Figure 8.6: Vortex line density vs time corresponding to Fig. 8.5 (Schwarz 1988).

$$\epsilon(t) = \epsilon(0)e^{\sigma t}, \tag{8.9}$$

that is to say, if $\sigma > 0$ the amplitude of the Kelvin wave will grow exponentially, as shown in Figure 8.7.

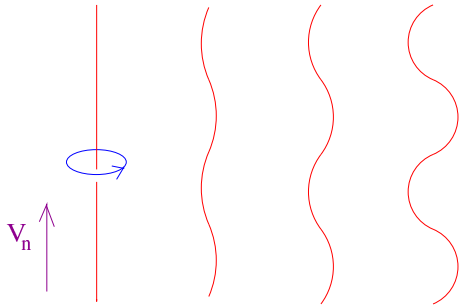

Figure 8.7: Donnelly–Glaberson instability.

In general, an arbitrary disturbances on a vortex line can be decomposed over modes with wavenumbers k. Initially, at small amplitude, each mode will grow or decay independently. We are interested in the mode which grows faster, because it will dominate all other modes. The maximum growth rate, σ_{max}, is obtained by setting $d\sigma/dk = 0$; we find

$$\sigma_{max} = \alpha \frac{V_{ns}^2}{4\beta}, \tag{8.10}$$

corresponding to the wavenumber $k_{max} = V_{ns}/(2\beta)$.

This instability plays an important role in the dynamics of a vortex tangle because it feeds energy from the normal fluid into quantised vorticity.

8.4 Classical aspects of quantum turbulence

Our understanding of ordinary homogeneous, isotropic turbulence (such as the turbulence away from walls in a wind tunnel) is based on the idea that energy is fed into the turbulence at large scale ℓ_0, and transferred to smaller and smaller scales by inertial instabilities (with no role played by viscous forces). At sufficiently small scale ℓ_1, called the Kolmogorov length scale, viscous forces become of the same order of magnitude as inertial forces, and, at scales smaller than ℓ_1, viscosity dissipates kinetic energy into heat. It is convenient to consider this process in the wavenumber space. Let k be the magnitude of the wave vector $\mathbf{k}$. It is found that the energy spectrum, $E(k)$, in the inertial range $1/\ell_0 \ll k \ll 1/\ell_1$ obeys the Kolmogorov scaling $E(k) \sim k^{-5/3}$, as shown in Fig. 8.8.

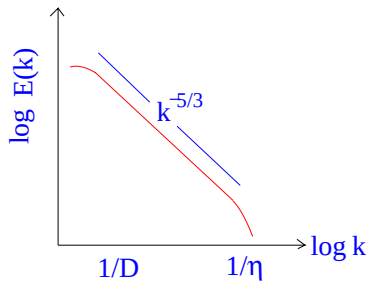

Figure 8.8: Kolmogorov energy spectrum $E(k) \sim k^{5/3}$ vs wavenumber k.

A number of recent experiments have revealed many classical aspects of quantum turbulence. For example, Walstron *et al.* (1998) forced helium II at high velocities along pipes and channels and observed the same pressure drops which are detected in ordinary turbulence. Smith *et al.* (1993) observed the same drag crisis in helium II which is seen in an ordinary fluid when a sphere moves at high velocity. Maurer and Tabeling (1998), who used counter–rotating propellers to continually excite turbulence in helium II, measured the energy spectrum, and found the classical Kolmogorov $-5/3$ scaling over

the entire temperature range explored, from T_λ down to $T = 1.4$ K. Numerical simulations of vortex tangles in the absence of friction produced similar energy spectra, see Nore *et al.* (1997), Araki *et al.* (2002), Kobayashi and Tsubota (2005). Experiments on the decay of quantum turbulence behind a towed grid (Smith *et al.* 1993) found that the temporal decay of turbulence in helium II behind a towed grid has the same $t^{-3/2}$ power law which is expected in an ordinary fluid from the Kolmogorov spectrum. The same time dependence of turbulence decay was found in counterflow turbulence (Barenghi and Skrbek 2007).

The current interpretation of these experiments is that at length scales larger than the intervortex spacing, the normal fluid and the superfluid are coupled by the friction and behave like a classical, ordinary fluid (Vinen and Niemela 2002, Hulton *et al.* 2002).

8.5 Quantum turbulence at absolute zero

At temperatures below 0.7 K, the normal fluid is negligible and helium II can be considered a pure superfluid. The question is what should be the properties of this special kind of turbulence. For example, it is apparent from numerical calculations of Tsubota that, without friction, the vortex tangle looks more "crinkled". Quantum turbulence experiments at temperatures as low as few mK were performed by Davis *et al.* (2000) using a vibrating grid; they found that the turbulence decays rapidly. This result was at first surprising. In ordinary fluids, turbulence decays without a continuous supply of kinetic energy because energy is dissipated by viscous forces at very small scales. In helium II, if the temperature is small enough that friction and viscous effects are negligible, it was not clear what this energy sink should be.

The numerical calculation by Nore *et al.* (1997) shed light onto the problem. They computed the evolution of a tangle of vortices using the GP equation, and observed that the kinetic energy decreases with time, while the sound energy increases (the total energy being constant). The sink of kinetic energy was thus found: it the generation of sound.

Further work revealed more details of the generation of sound energy by vortices and the classical aspect of the problem, i.e. vortex sound is well–known in classical fluid dynamics. In the context of superfluids, numerical simulations performed using the GP equation revealed that quantised vortices radiate sound energy when they accelerate. For example, Barenghi *et al.* (2005) found that a 2–dimensional vortex–antivortex pair which interacts with an isolated vortex changes suddenly the direction of motion and emits

a ripple of sound waves, as shown in Figure 8.9. After the interaction, the vortex–antivortex is smaller because it has less kinetic energy.

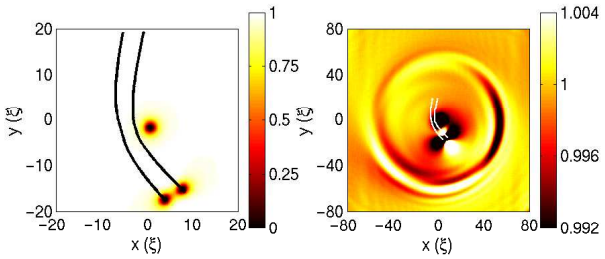

Figure 8.9: Left: vortex–antivortex pair which approaches a third isolated vortex and becomes deflected. Right: the sound ripple (small density oscillations) which are generated. The trajectory of the vortex pair is superimposed.

By studying numerically the collision of vortex rings in the GP equation as in Figure 8.10, Leadbeater *et al.* (2001) discovered a more fundamental aspect of the transformation of kinetic energy into sound: a rarefaction pulse is emitted at each vortex reconnection event. The pulse is short (few healing lengths), intense (initially, at the reconnection, the density drops to zero), and localized with respect to the angle of the reconnection. The pulse removes kinetic energy from the vortex configuration. Unlike vortex sound, this effect has no classical counterpart: vortices in a classical inviscid Euler fluid cannot reconnect (changes in topology are forbidden by the conservation of helicity); vortices in a classical viscous Navier–Stokes fluid can reconnect, but, being viscous, are not relevant to our problem. Figure 8.10 shows the collision of vortex rings, and Figure 8.11 the sound pulse which is generated. Within a dense vortex tangle, quantised vortices lose energy both ways, through radiation and reconnection pulses, as shown in Figure 8.12.

By studying numerically the collision of vortex rings in helium II, in typical experimental conditions, the vortex line density is not large enough for the decay of kinetic energy to be explained by vortex reconnections alone. Vinen considered the sound classically radiated by simple vortex configurations such as vortex pairs and Kelvin waves. He found that the power which is radiated per unit length by a co–rotating vortex–vortex pair separated by the distance ℓ is proportional to ℓ^{-6}. Taking for ℓ the average intervortex spacing deduced from the observed vortex line density, Vinen concluded that sound radiation by moving vortices cannot account for the observed decay of superfluid turbulence: a much shorter length scale is necessary to radiate enough sound and explain the measurements.

The mechanism to shift kinetic energy to shorter and shorter length scales, short enough that sound can be radiated away, is the Kelvin wave cascade

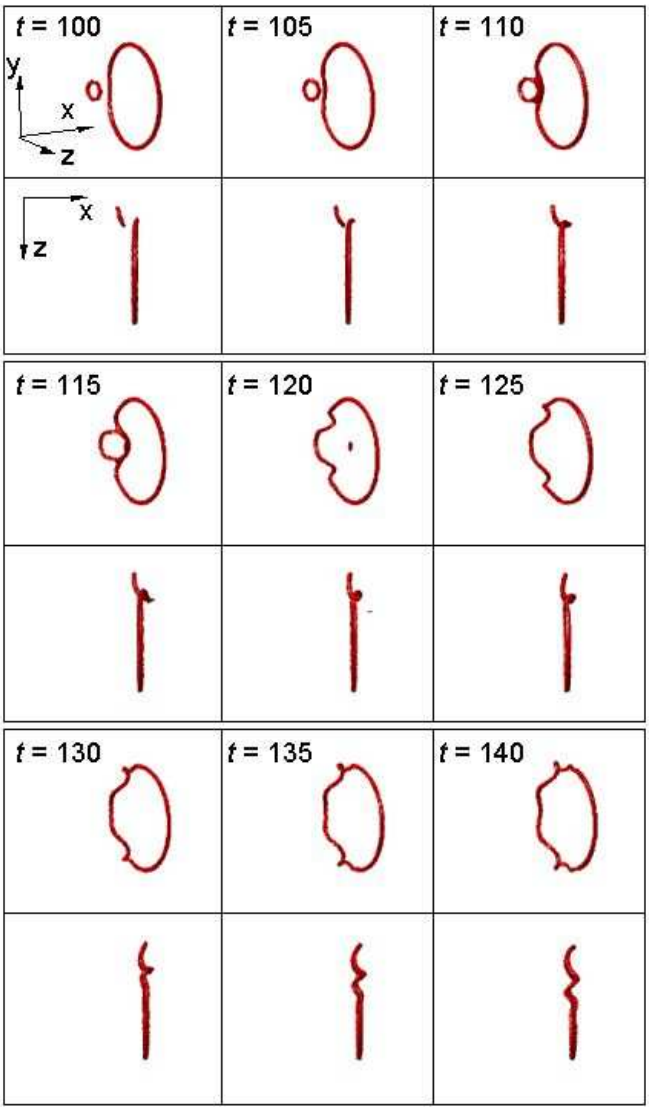

Figure 8.10: Collision of vortex rings. The time sequence shows two views of the colliding rings. The dot visible at $t = 120$ is the rarefaction pulse.

.

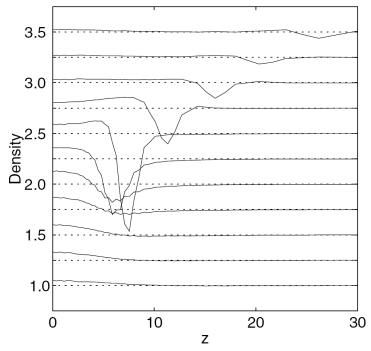

Figure 8.11: Density along the z–axis for a collision of two vortex rings initially offset with respect to each other. The curves correspond to different times and are offset with respect to each other for clarity. Just before the reconnection (bottom curve) the density is uniform except for a slight increase near the origin indicating the approaching rings. At the reconnection a rarefaction pulse is created at the centre of which the depth drops to zero. As the pulse moves away, the depth decreases and the pulse becomes more shallow

.

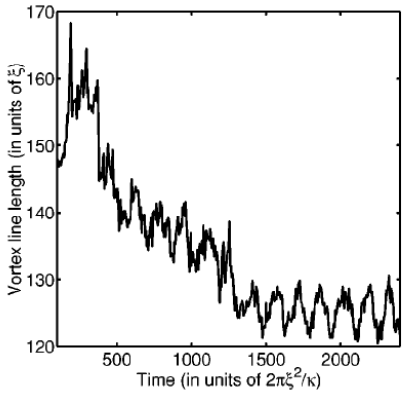

Figure 8.12: Vortex length vs time. The sudden drop corresponds to the emission of a rarefaction pulse, the decaying oscillations to sound radiation.

(Kivotides *et al.* 2001, Kozik and Svistunov 2005) The Kelvin wave cascade has some analogy with the classical Richardson cascade. The following numerical calculation by Kivotides *et al.* (2001) showed how vortex reconnections trigger the cascade. Figures 8.13, 8.14, 8.15 and 8.16 show four vortex rings which collide and undergo vortex reconnections. The cusps produced at the reconnections relax, and the nonlinear interaction of large amplitude Kelvin waves generate Kelvin waves at shorter and shorter scales, until the resulting energy spectrum saturates - see Figure 8.17. Current theoretical work by L'vov *et al.* (2007) on the problem is concerned with the possibility of a bottleneck between the classical Kolmogorov spectrum (at wavenumbers $k \ll 1/\ell$) and the Kelvin wave spectrum (at wavenumbers $k \gg 1/\ell$).

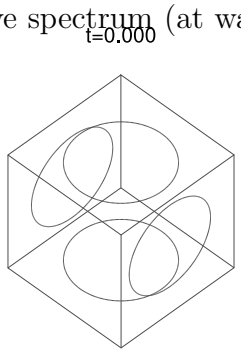

Figure 8.13: Kelvin wave cascade, $t = 0.0$ s: just before vortex reconnections.

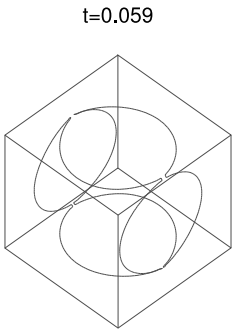

Figure 8.14: Kelvin wave cascade, $t = 0.059$ s: just after vortex reconnections.

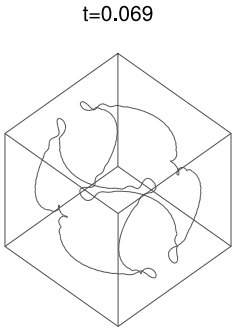

Figure 8.15: Kelvin wave cascade, $t = 0.129$ s: note the large amplitude Kelvin waves.

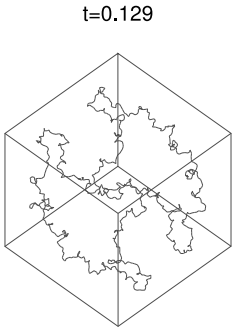

Figure 8.16: Kelvin wave cascade, $t = 0.129$ s: note the very short wavelengths.

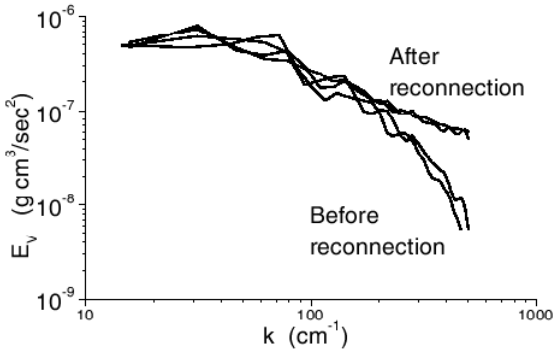

Figure 8.17: Kelvin wave cascade: the energy spectrum before the vortex reconnections and after saturation.

Chapter 9

References

Books

• J.F. Annett, *Superconductivity, superfluidity and condensates*, Oxford U. Press (2004)
• C.F. Barenghi, R. J. Donnelly and W.F. Vinen, eds., *Quantized Vortex Dynamics and Superfluid Turbulence*, Springer (2001),
• C.F. Barenghi and Y.A. Sergeev, eds., *Vortices and Turbulence at Very Low Temperatures*, Springer (2008),
• R. J. Donnelly, *Quantized Vortices In Helium II*, Cambridge University Press (1991).
• A.M. Guenault, *Basic Superfluids* Taylor & Francis (2002).
• L. D. Landau and E. M. Lifshitz, *Fluid Mechanics. Course of Theoretical Physics, Vol. 6.* Butterworth-Heinemann, 1987.
• P.V.E. McClintoco, D.J. Meredith and J.K. Wigmore, *Matter at Low Temperatures*, Blackie & Son (1984).
• C. J. Pethick and H. Smith, *Bose-Einstein Condensation In Dilute Gases*, Cambridge University Press, Cambridge (2001).
• T. Shachtman, *Absolute Zero and the Conquest of Cold*, Houghton Mifflin Company (1999).

Articles

• D. R. Allum, P. V. E. McClintock, A. Phillips and R. M. Bowley, Phil. Trans. Roy. Soc. London A **284**, 179 (1977).
• T. Araki, M. Tsubota, and S. K. Nemirovskii, Phys. Rev. Lett. **89**, 145301 (2002).
• C. F. Barenghi, R. J. Donnelly, and W. F. Vinen, J. Low Temp. Physics **52**, 189 (1983).

• C. F. Barenghi, N. G. Parker, N. P. Proukakis, and C. S. Adams, J. Low Temp. Physics, **138**, 629 (2005).
• C. F. Barenghi and L. Skrbek, J. Low Temp. Physics **146**, 5 (2007).
• G. P. Bewley, D. P. Lathrop, and K. R. Sreenivasan, Nature, **44**, 588 (2006).
• D. K. Cheng, M. W. Cromar, and R. J. Donnelly, Phys. Rev. Lett. bf 31, 433 (1973).
• S. I. Davis, P. C. Hendry, and P. V. E. McClintock, Physica B, **280**, 43 (2000).
• R. P. Feynman. In C. J. Gorter, editor. *Progress in Low Temperature Physics, Vol. 1.* North-Holland, Amsterdam, p. 17, 1955.
• T. Frish, Y. Pomeau, and S. Rica, Phys. Rev. Lett. **69**, 1644 (1992).
• H. E. Hall and W. F. Vinen, Proc. R. Soc. London, Ser. A **238**, 215 (1956).
• S. Hulton, C. F. Barenghi, and D. C. Samuels, Phys. Rev. Lett. **89**, 275301 (2002).
• D. Kivotides, J. C. Vassilicos, D. C. Samuels, and C. F. Barenghi, Phys. Rev. Lett., **86**, 3080 (2001).
• M. Kobayashi and M. Tsubota, Phys. Rev. Lett. **94**, 065302 (2005).
• J. Koplik and H. Levine, Phys. Rev. Lett. **71**, 1375 (1993).
• E. Kozik and B. Svistunov, Phys. Rev. B **72**, 172505 (2005).
• M. Leadbeater, T. Winiecki, D. C. Samuels, C. F. Barenghi, and C. S. Adams, Phys. Rev. Lett. **86**, 1410 (2001).
• V. S. L'vov, S. Nazarenko, and O. Rudenko, Phys. Rev. B **76**, 024520 (2007).
• K. W. Madison, F. Chevy, W. Wohlleben, and J. Dalibard, Phys. Rev. Lett. **84**, 806 (2000).
• J. Maurer and P. Tabeling, Europhys. Lett. **43**, 29 (1998).
• D. J. Melotte and C. F. Barenghi, Phys. Rev. Lett. **80**, 4181 (1998).
• C. Nore, M. Abid, and M.-E. Brachet, Phys. Rev. Lett. **78**, 3896 (1997).
• R. M. Ostermeier and W. I. Glaberson, J. Low. Temp. Phys. **21**, 191 (1975).
• L. Onsager, Nuovo Cim. Suppl. 2 **6**, 249 (1949).
• K. W. Schwarz, Phys. Rev. B **38**, 2398 (1988).
• M. R. Smith, R. J. Donnelly, N. Goldenfeld, and W. F. Vinen, Phys. Rev. Lett. **71**, 2583 (1993).
• M. R. Smith, D. K. Hilton, and S. V. Van Sciver, Phys. Fluids, **11**, 751 (1999).
• J.T. Tough, "Superfluid Turbulence", in *Progress in Low Temperature Physics*, vol. VIII, ed. by D.F. Brewer, North Holland, Amsterdam, pg. 133.

• W. F. Vinen, Proc. Roy. Soc. London A **240** 114 (1957); **240** 128 (1957); **242** 493 (1957); **243** 400 (1957).
• W. F. Vinen and J. J. Niemela, J. Low Temp. Phys. **128**, 167 (2002), and Erratum, **129**, 213 (2002).
• P. L. Walstrom, J. G. Weisend, J. R. Maddocks, and S. V. Van Sciver, Cryogenics **28**, 101 (1998).
• G. A. Williams and R. E. Packard, Phys. Rev. Lett. **33**, 280 (1974).
• T. Winiecki and C. S. Adams, Europhysics Lett. **52**, 257 (2000).
• Nature Physics, **1**, 36 (2005).